

Shear-slip behaviour of prefabricated composite shear stud connectors in composite bridges

Gao, Yanmei; Li, Chengjun; Wang, Xuefei; Zhou, Zhixiang; Fan, Liang; Heng, Junlin

DOI

[10.1016/j.engstruct.2021.112148](https://doi.org/10.1016/j.engstruct.2021.112148)

Publication date

2021

Document Version

Accepted author manuscript

Published in

Engineering Structures

Citation (APA)

Gao, Y., Li, C., Wang, X., Zhou, Z., Fan, L., & Heng, J. (2021). Shear-slip behaviour of prefabricated composite shear stud connectors in composite bridges. *Engineering Structures*, 240, 1-16. Article 112148. <https://doi.org/10.1016/j.engstruct.2021.112148>

Important note

To cite this publication, please use the final published version (if applicable). Please check the document version above.

Copyright

Other than for strictly personal use, it is not permitted to download, forward or distribute the text or part of it, without the consent of the author(s) and/or copyright holder(s), unless the work is under an open content license such as Creative Commons.

Takedown policy

Please contact us and provide details if you believe this document breaches copyrights. We will remove access to the work immediately and investigate your claim.

1 Shear-Slip Behaviour of Prefabricated Composite Shear Stud Connectors 2 in Composite Bridges

3 Yanmei Gao¹, Chengjun Li², Dong Liu¹, Zhixiang Zhou³, Liang Fan¹, Junlin Heng^{3,4}

4 ¹ Department of Bridge Engineering, School of Civil Engineering, Chongqing Jiaotong University,
5 Chongqing 400074, China

6 ² Department of Road and Bridge Engineering, Sichuan Vocational and Technical College of
7 Communications, Chengdu 611130, China

8 ³ Department of Civil Engineering, College of Civil and Transportation Engineering, Shenzhen
9 University, Shenzhen 518060, China

10 ⁴ Department of Engineering Structures, School of Civil Engineering and Geosciences, Delft
11 University of Technology, Delft 2628 CN, The Netherlands

12 **Abstract:** This paper has investigated the shear-slip behaviour of an innovative prefabricated composite
13 shear stud (PCSS) connector and its application in the prefabricated steel-concrete composite bridges.
14 A series of push-out tests are carried out on a total of 12 specimens, including 6 PCSS specimens and
15 6 conventional shear stud (CSS) specimens. Further comparison has been carried out between the test
16 result and the data available from the literature. Based on the test, a high-resolution finite element (FE)
17 analysis has been performed to reveal the load transfer mechanism of the PCSS connector at the
18 component-level. After that, an advanced FE model has been established and validated by a full-scale
19 test of the prefabricated composite bridge using the PCSS. With the FE model, the load-slip behaviour
20 and slip distribution are investigated in details. The result highlights the enhanced shear capacity and
21 ductility of the PCSS specimens compared with the CSS specimens, as well as the feasibility of PCSS
22 connectors in composite bridges. Meanwhile, it is further revealed by the detailed investigation that the
23 enhancement could be attributed to the lateral constraint on the concrete by the vertical steel plate in
24 the PCSS. Besides, it is also found that the load-slip behaviour of composite bridges using the PCSS is
25 influenced by the cracking at the seam between deck blocks. Consequently, abrupt changes can be
26 found in the load-slip curve once the cracking occurs, which differs from the traditional composite
27 bridges.

28 **Keywords:** prefabricated composite shear studs connector; prefabricated steel-concrete composite
29 bridge; push-out test; high-resolution finite element analysis; shear-slip behaviour; load-transfer
30 mechanism.

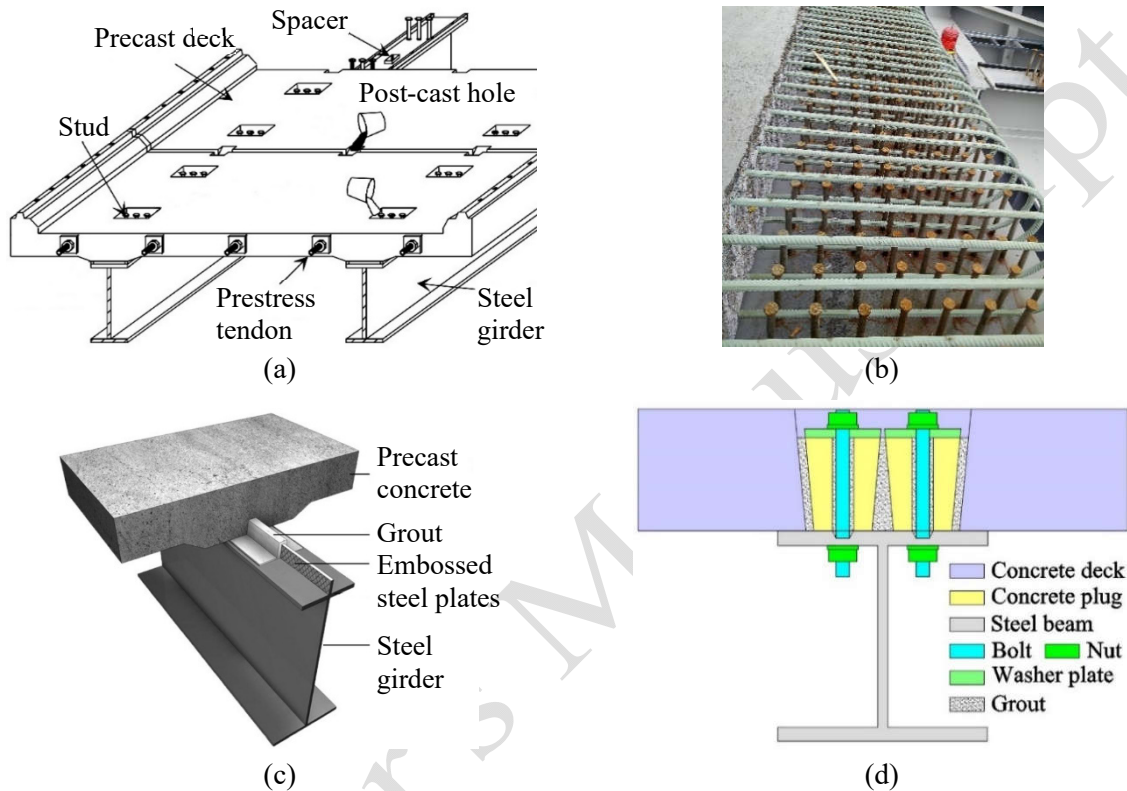
31 **1. Introduction**

32 Steel-concrete composite bridges are extensively applied worldwide since they efficiently utilise
33 mechanical features of both the steel and concrete materials. The concrete bridge deck is usually
34 connected to the steel structures through shear connectors, by which the two members can work together
35 compatibly [1]. Apart from the advantages, several challenges remain in the application of accelerated
36 bridge construction (ABC) in composite bridges, especially in connecting the steel and concrete during
37 the in-site erection. Thus, extra efforts are required to build the composite bridge in the ABC way [2].
38 On this end, the pre-cast decks and in-site connections are gradually employed in composite bridges,
39 which can notably accelerate the construction and minimise the effect of shrinkage and creep in the
40 concrete deck [3]-[8].

41 Extensive research efforts have been made by researchers worldwide respecting the application of
42 pre-cast concrete decks in composite bridges, and several types of shear connectors were proposed in
43 accordance. As per the configuration and mechanical features, the proposed shear connectors can be
44 divided into 4 types, including the clustered shear stud connector, distributed shear stud connector, and
45 embossed steel plate connector and friction-based shear connector, as shown in Figs. 1a to d.

46 The clustered shear stud connector (shown in Fig. 1a) is currently the most popular type due to its
47 matureness in engineering practices. In the connector, the studs are arranged group-by-group at multiple
48 locations on the top surface of steel members. In the erection, the concrete deck is at first prefabricated
49 in the casting yard with a series of post-cast holes reserved. After that, the pre-cast deck is installed on
50 the steel girder in the construction field, with the shear studs accommodated within the reserved holes.
51 Then the holes will be filled in with the cast-in-situ concrete to connect the deck and steel girder. To
52 date, considerable research efforts have been made on the clustered shear stud. Through static tests,
53 Shim et al. [9] investigated the influence of key design parameters on the mechanical performance of
54 shear studs. The studied parameters include the spacing between studs, hooping parameter and stud
55 diameter. According to the result, the ultimate strength of the connector decreases with the spacing
56 between studs, which can be considered by a proposed empirical equation. Xiang et al. [10] studied the
57 mechanical behaviour of composite beams with the different layout of studs, using the static test and
58 finite element analysis. The result suggested that no explicit relationship was found between the layout

59 of the studs and the loading capacity of composite beams. Wang et al. [11] carried out a series of tests
 60 to investigate the influence of the shape of the reserved holes, including the rectangular hole and circular
 61 hole. The result indicated that the mechanical performance of connectors is better with rectangular holes
 62 than with circular holes. Sjaarda et al. [12] conducted the fatigue test of the composite beam with cluster
 63 shear studs, indicating that the fatigue performance is compatible with the cast-in-situ deck.



64 **Fig. 1.** Four typical types of prefabricated shear connectors: (a) clustered shear stud connector -
 65 adapted from [9]; (b) distributed shear stud connector - courtesy of Dr Yanmei GAO; (c) embossed
 66 steel plate connector - adapted from [14]; (d) friction-based shear connector – adapted from [16].

67 The distributed shear stud connector is an alternative solution to the clustered shear stud connector
 68 [2]. As shown in Fig. 1b, the studs are uniformly placed along the longitudinal direction of the deck,
 69 and the continuous post-cast strip is left to accommodate the studs instead of the hole. Compared with
 70 clustered studs, the distribution of shear force becomes more even in distributed studs due to the
 71 decentralization. As a result, the concrete deck works with the steel girder in a more compatible way.
 72 However, according to Liu et al. [13], the mechanical behaviour of the composite bridge using
 73 distributed studs is almost the same as the one using clustered studs. It is worth noting that the
 74 distributed shear stud was proposed by FWHA [15] as the standard design for the steel-concrete
 75 connection in prefabricated steel-concrete composite bridges.

76 The embossed steel plate connector [14] is different from the above two connectors using studs.
77 As shown in Fig. 1c, the embossed steel plate is vertically welded to the top surface of the steel beam,
78 which will be accumulated by the reserved post-cast strip when assembling. The post-cast strip is then
79 filled in with the high-grade grout to combine the vertical steel plate with the concrete deck. According
80 to the static and fatigue tests, the mechanical capacity of the embossed steel plate connector is almost
81 the same as that of the shear stud-based connectors.

82 The layout of the friction-based shear connector (FBSC) [16] is similar to the clustered shear stud
83 connector, as shown in Fig.1d, except that preloaded bolts are used instead of shear studs. As a result,
84 the shear force between the deck and steel member is transferred through the friction force rather than
85 the deformation of studs. As per the push-out tests of 11 specimens, it was claimed that a higher shear
86 capacity could be expected in the FBSC compared with the shear stud connector.

87 A common feature of the above connectors is that the post-cast hole or strip should be reserved in
88 the pre-cast deck in advance. As per the relevant studies [9], [17], cracks are highly prone to initiate
89 from the corner of these post-cast holes or strips. The cracking can be mainly attributed to the following
90 two factors: (1) high-level stress concentration exists in the corner of the holes or strips due to the age
91 difference between the pre- and post-cast concretes; (2) the prestress applied by tendons cannot be
92 effectively transferred to the shear holes or strips. Meanwhile, cracks are also likely to initiate in the
93 cast-in-situ seam between different segments of the deck, which mainly depends on the quality of the
94 post-cast mortar and the effective prestress.

95 Recently, several types of post-casting-free shear connectors were proposed for building
96 structures, including the through-bolt connector [18][19] and friction-grip bolt connector [20].
97 However, these connectors are not feasible with the employment of the prestress, which largely limits
98 their application in composite bridges.

99 In dealing with the discussed issues, an innovative prefabricated composite shear stud (PCSS)
100 connector has been proposed [21][22]. In the PCSS, no post-cast work is required, and the prestress can
101 be easily applied in the concrete deck in an efficient way. The feasibility of the PCSS connector has
102 been preliminarily verified through the fabrication experiment [23]. However, due to the limited number

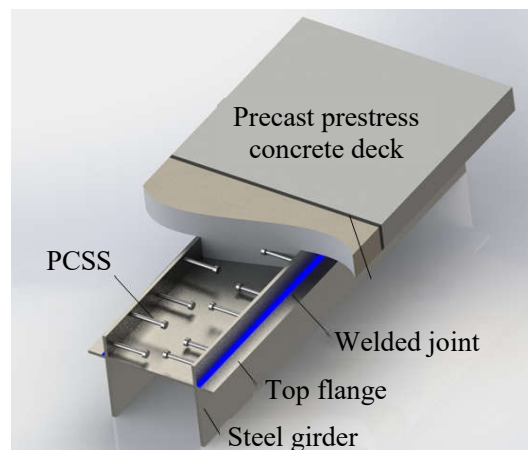
103 of specimens, the shear-slip behaviour, which reflects the load transfer between the concrete and steel,
104 has not yet been illustrated in detail for the composite bridges using the PCSS.

105 This study aims to investigate the shear-slip behaviour of the PCSS connector and further reveal
106 the mechanism of load transfer between the concrete and steel in composite bridges using the PCSS. In
107 Section 2, a total of 12 push-out specimens have been tested, including 6 PCSS specimens and 6
108 specimens with conventional shear stud (CSS) connectors. Based on the present test and the data from
109 the literature, further comparison has been made on the shear-slip behaviour between the PCSS and the
110 CSS. Moreover, high-resolution finite element (FE) analysis has been conducted to reveal the
111 mechanical behaviour of the PCSS specimen. In Section 3, further investigation has been carried out
112 on the distribution of the slip and load transfer mechanism in the composite bridge using the PCSS,
113 including both the full-scale model test and refined FE analysis. In Section 4, the major conclusions are
114 drawn from the study. In summary, the outputs can serve as the guideline for the research, design and
115 fabrication of composite bridges using PCSS connectors.

116 2. Push-out test of PCSS connector

117 2.1 Innovation of the PCSS connector

118 The prefabricated composite shear stud (PCSS) connector is proposed to improve the application
119 of ABC in composite bridges, as shown in Fig. 2. The PCSS connector consists of two steel plates, with
120 a series of distributed shear studs welded on. When casting the concrete deck, the two vertical steel
121 plates serve as sheets, with the studs embedded in the concrete. Then the prestress is applied to the deck
122 through tendons after the deck is installed in place.



123
124

Fig. 2. Design of the prefabricated composite shear stud connector.

125 It is worth noting that the steel girder and concrete deck are not connected during the pretension,
 126 so that the prestress can be effectively transferred to the concrete deck. After that, the two steel plates
 127 are welded to the top flange of the steel girder, through which the deck and the steel girder are
 128 connected. Apparently, the post-casting hole or strip is no longer required when using the PCSS. As a
 129 result, the configuration of the deck is notably simplified as well as the fabrication process. Moreover,
 130 the post-cast concrete is replaced by the welded connection, whose quality is easier to control by the
 131 application of proper welding technology and quality assurance. As a result, the PCSS is expected to
 132 eliminate the cracking issue of the concrete deck induced by the age difference.

133 2.2 Design of comparative push-out tests

134 2.2.1 Configuration of specimens

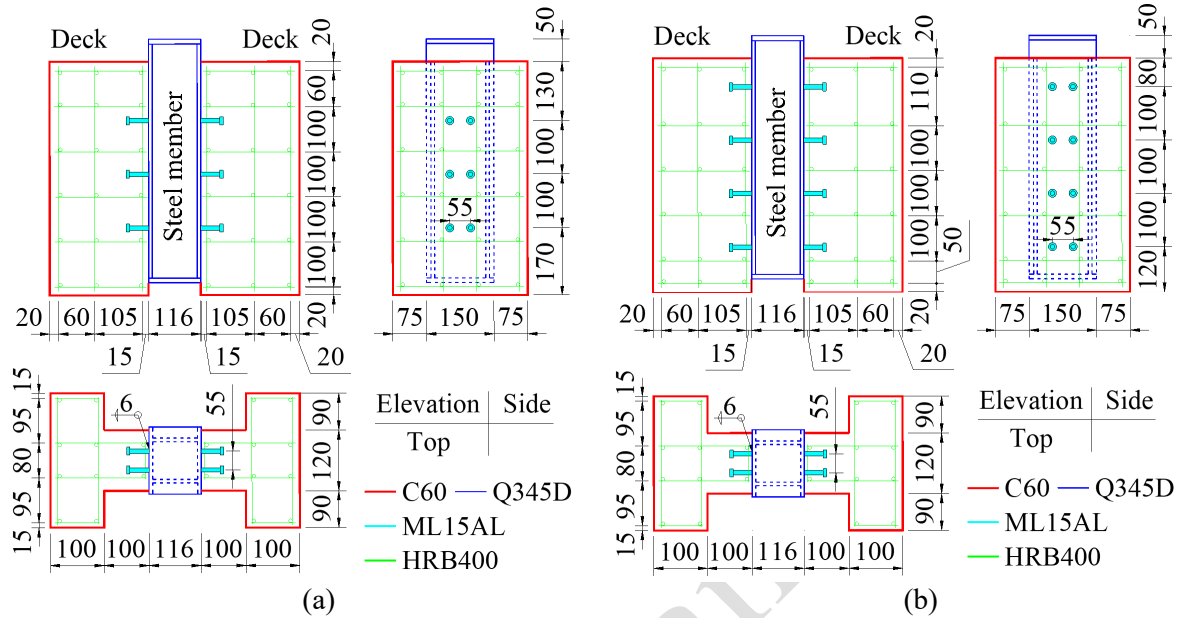
135 A series of comparative push-out tests are carried out to investigate the shear-slip behaviour of the
 136 novel PCSS connector, including a total of 12 specimens. The specimens are respectively fabricated
 137 with two types of connectors, i.e., the PCSS and conventional shear stud (CSS). Within each type, the
 138 specimens can be classified into two groups by the row of studs, i.e., 3 or 4 rows. Table 1 shows the
 139 details about the classification of the specimens.

140 **Table 1** Classification of specimens

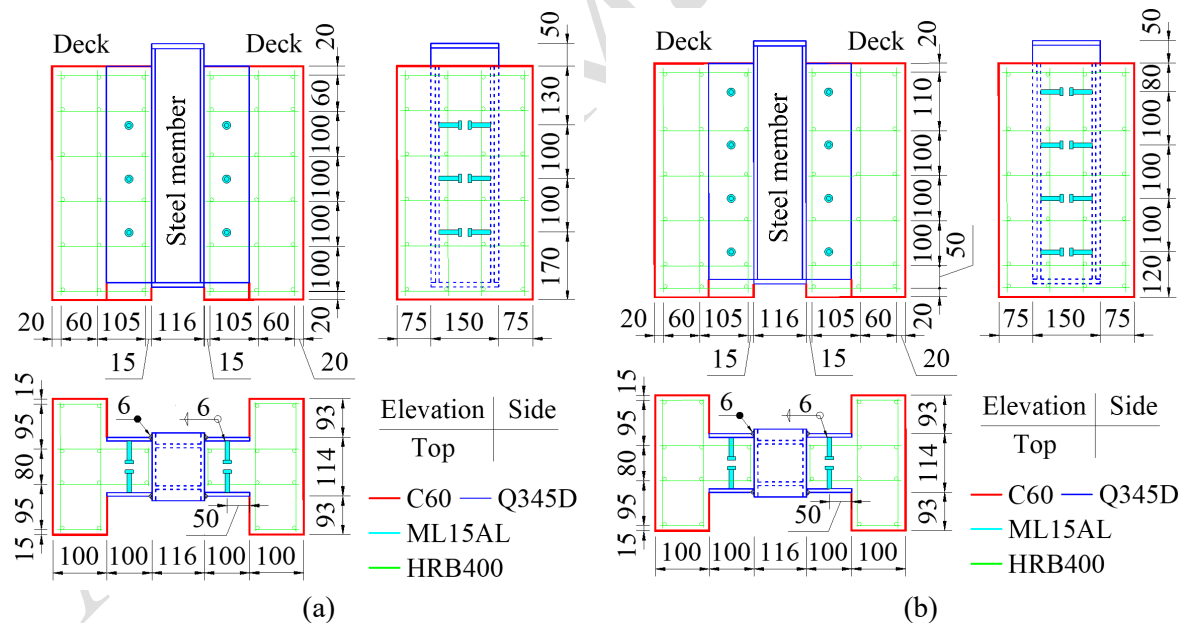
Type	Group	Stud layout	Row of studs	Connection	Number of specimens
PCSS	HS3	Horizontal	3	Welding	3
	HS4	Horizontal	4	Welding	3
CSS	VS3	Vertical	3	Casting-in-situ	3
	VS4	Vertical	4	Casting-in-situ	3

141 It is worth noting that, the PCSS specimens are fabricated with the horizontal stud (HS), while the
 142 vertical stud (VS) is employed in the CSS specimens. For better illustration, the specimens are named
 143 after the layout and number of studs, followed by the serial number of the specimen within the group.
 144 The configuration of the CSS and PCSS specimens are shown in Figs. 3 and 4, respectively. The
 145 specimen consists of a hollow steel box in the middle and a T-shaped concrete deck at both sides,
 146 connected either by the PCSS or CSS. The steel box is 530 mm long, 150 mm wide and 116 mm deep,
 147 with the plate thickness of 8 mm. Meanwhile, the concrete deck is 500 mm long, 300 mm wide and 200
 148 mm deep, with the reinforcement of 8 mm in diameter. In both the type of connections, the size of studs

149 is $\Phi 10 \text{ mm} \times 50 \text{ mm}$, i.e., 10 mm in diameter and 50 mm in height. At the top of the stud, a 7 mm-thick
 150 cap is designed to prevent the concrete from pulling up, with an enlarged diameter of 18 mm. In the
 151 PCSS specimen, the vertical steel plate is 100 mm-high and 8 mm-thick, to which the studs are welded.



152 **Fig. 3.** Layout of CSS specimen (Unit: mm): (a) VS3; (b) VS4.



153 **Fig. 4.** Layout of PCSS specimen (Unit: mm): (a) HS3; (b) HS4.

154 Different fabrication procedures are employed for the PCSS and CSS specimens, respectively. In
 155 the CSS specimen, the studs are directly welded to the top flange of the steel box and then covered
 156 within the concrete deck when casting. In the PCSS specimen, the studs are at first welded to the vertical
 157 steel plate. The concrete deck is then cast between vertical plates, with the studs embedded. Finally, the

158 deck is connected to the top flange of the steel box through the fillet welded joint, as shown in Fig. 2.
 159 In both types of specimens, continuous fillet welded joints are employed to connect the studs with the
 160 steel plate, with a weld leg length of 6 mm. Similarly, the fillet welded joint has also been employed in
 161 the vertical plate-to-flange connection in the PCSS specimens, with a length of 6 mm. The welds are
 162 performed by flux-cored arc welding (FCAW) protected with CO₂, using the manual welding machine.

163 In the fabrication, the structural steel Q345D [24] is used for the steel member and the vertical
 164 plate, while the cold-forging steel M15AL [24] is chosen for the shear studs as per the rule of
 165 performance protection. The deck is made of the concrete C60 [25], with the reinforcement of the steel
 166 bar HRB400 [25]. Prior to the push-out test, static material tests have been carried out to obtain the
 167 basic mechanical properties of the testing materials. The measured material data are shown in Table 2.

168 **Table 2** Measured mechanical properties of the testing materials

Shear stud			Steel box/plate		Reinforcement		Concrete deck	
Elastic modulus (GPa)	Yielding strength (MPa)	Ultimate strength (MPa)	Elastic modulus (GPa)	Yielding strength (MPa)	Elastic modulus (GPa)	Yielding strength (MPa)	Elastic modulus (GPa)	Cubic strength (MPa)
205	340	430	195	365	209	458	34.6	62.1

169 2.2.2 Test Setup

170 Static loading tests have been carried on the specimens using a hydraulic testing machine with a
 171 maximum capacity of 10,000 kN, as shown in Fig. 5. During the test, electronic dial gauges have been
 172 installed between the root of studs and the concrete to measure the relative displacement between the
 173 concrete deck and the steel box, i.e., the slip. The installed dial gauges have a maximum range of 10
 174 mm and a resolution of 0.001 mm. Before loading, a target force F_t has been calculated using an analytic
 175 model proposed to solve the ultimate capacity in [24]. According to the model, the ultimate capacity of
 176 the specimen is controlled by the shear fracture of studs. At the same time, the failure of studs will also
 177 be influenced by the concrete surround them, as shown in Equation 1.

$$178 \quad N_t^c = \sum_{v=1}^{n_{std}} N_v^c \quad (1a)$$

$$179 \quad N_v^c = 1.19 A_{std} f_{std} (E_c/E_s)^{0.2} (f_{cube}/f_{std})^{0.1} \quad (1b)$$

179 Where N_t^c and N_v^c are the total capacity and the capacity of single stud; n_{std} is the number of studs;
 180 A_{std} stands for the sectional area of studs; E_c and E_s are the elastic modulus of the concrete and stud;
 181 f_{cube} and f_{std} are respectively the cubic strength of the concrete and the uniaxial strength of the stud.

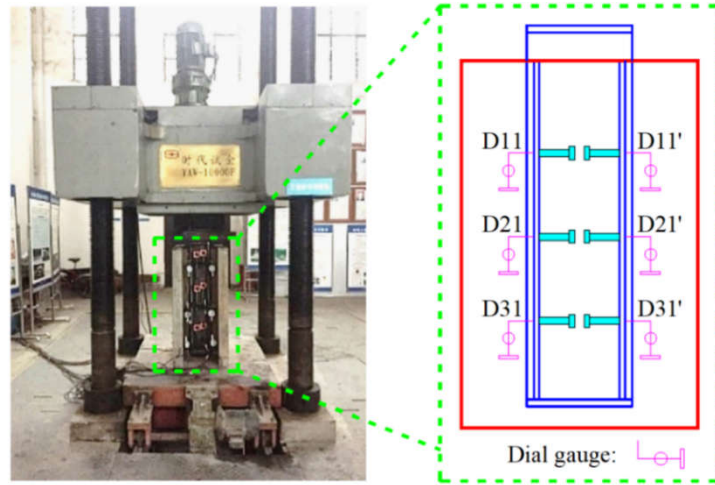


Fig. 5. Set up of the static loading test (HS3-2).

Based on the target force, a total of 5 loading cycles is applied to each specimen, as illustrated in Table 3. In the 1st loading cycle, a preload with 10% of the target force is loaded and unloaded. After that, 3 cycles with 30% of the target force are applied with an increment of 5%. In the final cycle, i.e. the 5th cycle, the specimen is loaded to failure with an increment of 10% of the target force. During the test, the measurement is carried out after each loading step. Besides, it is worth stating that in the 5th cycle, the applied loading force can be increased beyond the target load until the failure of the specimen is achieved.

Table 3 Loading prototypes

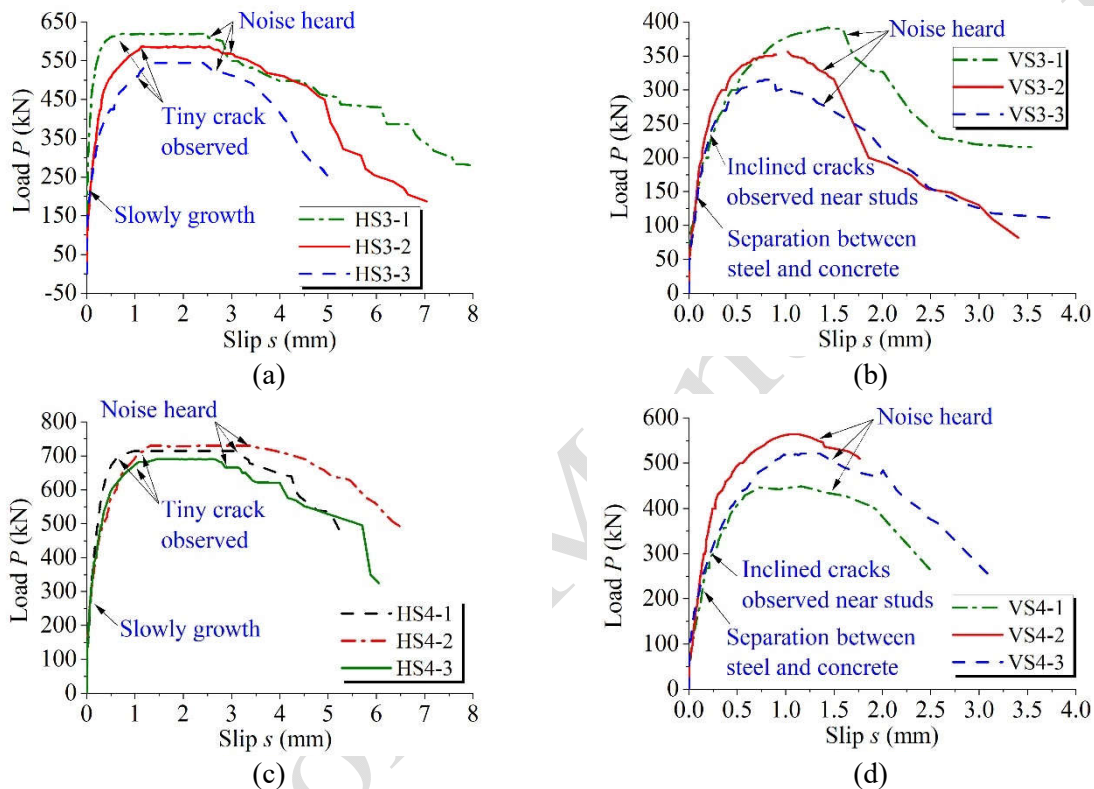
Loading cycle	Type	Prototype
1st	Preload	$0 \rightarrow 0.03F_t \rightarrow 0.06F_t \rightarrow 0.1F_t \rightarrow 0.06F_t \rightarrow 0.03F_t \rightarrow 0$
2nd ~ 4th	Cyclic	$0 \rightarrow 0.05F_t \rightarrow 0.1F_t \rightarrow 0.15F_t \rightarrow 0.2F_t \rightarrow 0.25F_t \rightarrow 0.3F_t$ $\rightarrow 0.25F_t \rightarrow 0.2F_t \rightarrow 0.15F_t \rightarrow 0.1F_t \rightarrow 0.05F_t \rightarrow 0$
5th	Ultimate	$0 \rightarrow 0.1F_t \rightarrow 0.2F_t \rightarrow 0.3F_t \rightarrow 0.4F_t \rightarrow 0.5F_t \rightarrow 0.6F_t \rightarrow 0.7F_t \rightarrow 0.8F_t \rightarrow 0.9F_t \rightarrow F_t$

2.3 Test results

2.3.1 Load-slip curve

Based on the measurement, the relation can be established respecting the load and the slip between the concrete deck and steel studs. The measured load-slip curves are illustrated in Figs. 6a to d, in which the average slip from the dial gauges in Fig. 5 is used. Generally, the curves can be divided into two stages, i.e., the ascending and descending stages. The ascending stage can be further classified as the linear and nonlinear parts, which are diverged at roughly 50% of the ultimate load.

199 Similarly, Oehlers and Bradford suggested the stud remains elastic before 50% of the ultimate load
 200 and the modulus could be regarded as a constant value [26]. Within the linear part, the slip increases
 201 slowly and proportionally with the applied load, indicating the elastic deformation of the specimen. The
 202 slip can be recovered after unloaded within the linear part, further demonstrating the pure elastic
 203 behaviour. When the load increases beyond 50% of the ultimate load, nonlinearity can be observed in
 204 the load-slip curve, indicating plastic deformation.

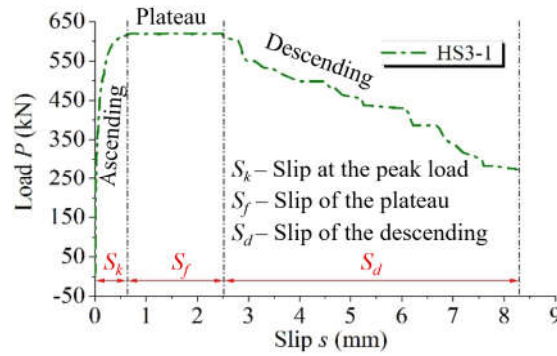


205 **Fig. 6.** Load-slip measured from the specimens: (a) HS3; (b) VS3; (c) HS4; (d) VS4.

206 In the PCSS specimens HS3 and HS4 series, tiny cracks have been observed in the concrete deck
 207 after the ultimate load is almost reached. After that, a flat plateau longer than 2 mm can be notably
 208 observed on the curve, suggesting the almost zero slope. At the end of the plateau, the fracture-like
 209 noise can be heard from the root of studs, suggesting the breaking of studs, as shown in Figs. 6a and c.
 210 Following the noise, the load starts to decrease while the slip continues increasing.

211 In the CSS specimens VS3 and VS4 series, the separation between the concrete and steel has been
 212 found at the end of the linear part in the curve. With the load increasing, inclined cracks can be soon
 213 found at the concrete near the studs, with a considerable length. Unlike the PCSS specimens, the
 214 fracture-like noise has been heard soon after the ultimate load is reached, and no apparent plateau can

215 be found in the derived curve. After that, the load will decrease at a high rate while the slip continues
 216 increasing, as shown in Figs. 6 b and d. The test results reveal that a higher peak load can be reached in
 217 the PCSS specimens compared with the CSS specimens. Meanwhile, the load decreases with a very
 218 steep slope after the ultimate load in the CSS specimen, compared with the PCSS specimens. In general,
 219 the load-slip curve can be divided into three stages according to the curvature, as shown in Fig 7.



220
 221 **Fig. 7.** Division of the load-slip curve (HS3-1).

222 For better comparison, the ultimate load and slip of each specimen are summarized in Table 4,
 223 along with statistics. The ultimate load includes not only the total value at the specimen level but also
 224 average per studs. The slip includes from the slip of the peak load S_k , the slip of plateau S_f and the slip
 225 of the descending stage S_d . According to the result, the mean ultimate load in the PCSS specimen is
 226 about 67.3% higher with 3 rows of studs and 39.1% higher with 4 rows of studs compared with the CSS
 227 specimen. Thus, a higher capacity per studs can be reached in PCSS specimens, as shown in Table 4.

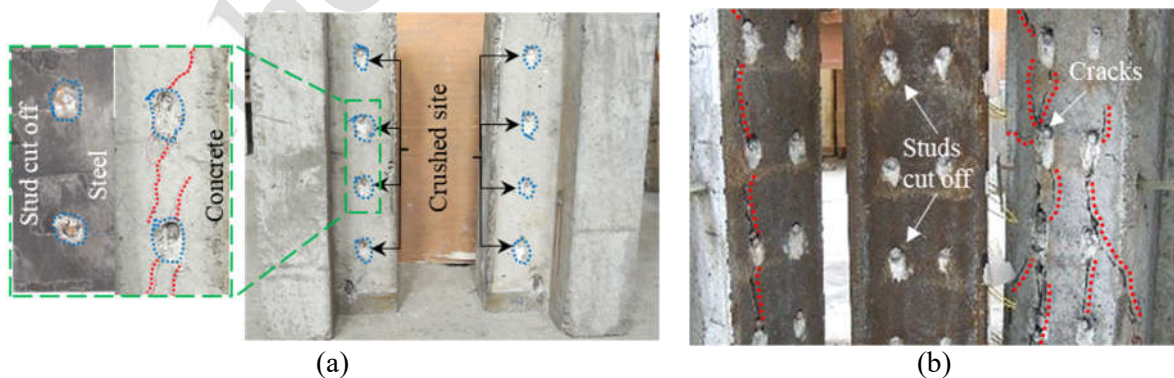
228 **Table 4** Summary of ultimate load and slip

Type	ID	Ultimate load P_u (kN)						Slip s (mm)			
		Specimen		Per studs		Peak S_k		Plateau S_p		Descending S_d	
		Test	Mean	Test	Mean	Test	Mean	Test	Mean	Test	Mean
CSS	VS3-1	388		32.3		1.33		-		1.95	
	VS3-2	356	349	29.7	29.1	1.02	1.12	-	-	2.43	2.44
	VS3-3	302		25.2		1.01		-		2.93	
	VS4-1	449		28.1		1.36		-		1.34	
	VS4-2	564	511	35.3	32.0	1.28	1.30	-	-	0.72	1.30
	VS4-3	521		32.6		1.25		-		1.84	
PCSS	HS3-1	620		51.7		0.73		1.75		5.78	
	HS3-2	587	584	48.9	48.6	1.13	1.23	1.89	1.57	4.02	4.18
	HS3-3	544		45.3		1.32		1.08		2.73	
	HS4-1	714		44.6		0.97		2.12		3.41	
	HS4-2	730	711	45.6	44.5	1.33	1.14	2.08	2.08	3.12	3.27
	HS4-3	690		43.1		1.12		2.05		3.27	

229 Apart from the loading capacity, in terms of the slip, PCSS specimens demonstrate a notably higher
 230 ductility compared with CSS specimens. At first, the two types of specimens show a similar slip value
 231 at the peak load, i.e. S_k , indicating the similar behaviour before the peak load. However, a very notable
 232 slip of plateau S_p could be found in the PCSS specimen, which is hard to be observed from CSS
 233 specimens. The mean value of S_p is 1.57 and 2.08 mm in the PCSS specimen with 3 rows and 4 rows
 234 of studs, respectively. For further evaluation on the ductility, the slip of descending stage S_d is also
 235 derived and listed in Table 4. The average S_d is 2.44 and 1.30 mm in CSS specimens with 3 and 4 rows
 236 of studs, respectively. Alternatively, the value is 4.18 mm in PCSS specimens with 3 rows of studs and
 237 3.27 mm in those with 4 rows, which is respectively 1.71 and 2.51 times the value in CSS specimens.
 238 Thus, a higher ductility could be expected by using the PCSS.

239 2.3.2 Failure model

240 The specimens have been cut after the test to investigate the failure model. Figs. 8a and b show
 241 the Macro-sectional view of the PCSS specimen HS4-3 and the CSS specimen VS4-1, respectively. In
 242 both types, the failure has been achieved with the studs cut off. However, the fractography in the
 243 concrete deck is different in the two types of specimens. In the PCSS specimens, the concrete deck has
 244 only been slightly crushed near the root of studs. As shown in Fig. 8a, only a few small cracks can be
 245 found around the studs, with a maximum crack width no more than 0.7 mm, and there was no penetrated
 246 crack found in all the PCSS specimens.



247 **Fig. 8.** Typical Macro-sectional view: (a) PCSS specimen HS4-3; (b) CSS specimen VS4-1.

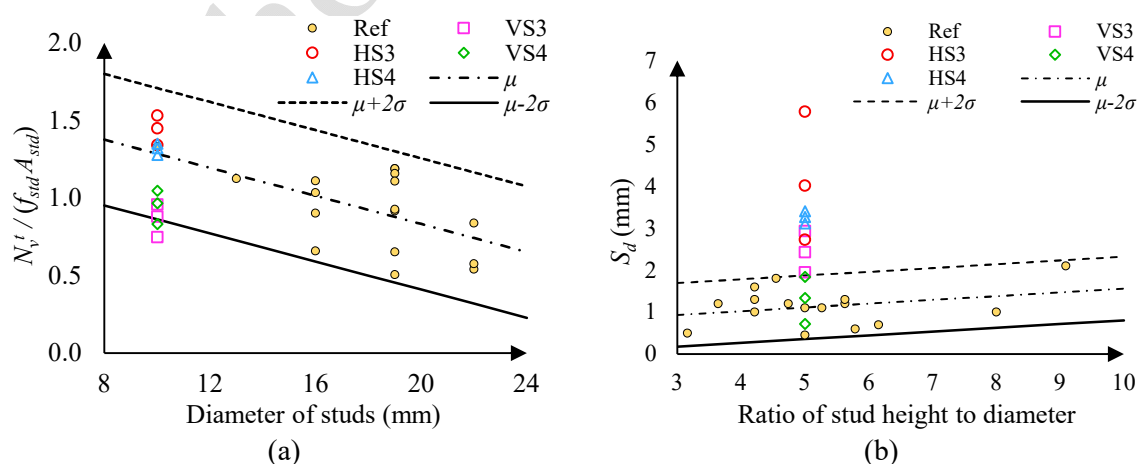
248 Alternatively, well-developed cracks can be observed in the CSS specimens, as shown in Fig. 8b.
 249 The concrete deck is seriously crushed with the inclined cracks initiated near the studs and propagated
 250 to the edge of the deck, with the maximum crack width of 3.5 mm. Meanwhile, most of the cracks in

251 the CSS specimens have penetrated through the thickness of the deck, and even some have already
 252 intersected.

253 It is worth stating that the section of the concrete deck could be responsible for the significant
 254 difference in the failure model between the PCSS and CSS specimens. In this study, the T-shaped deck
 255 is employed since it is highly fitted to the configuration of PCSS connectors. For better comparison, it
 256 is also used in the fabrication of CSS specimens. However, the volume of concrete around studs is
 257 reduced in the CSS specimen with T-shaped deck, compared with the one using the flat deck. As a
 258 result, the mechanical performance of near-stud concretes could be decreased in CSS specimen, due to
 259 the degradation in the constraint effect by nearby concretes. Thus, once the partial crushing occurred at
 260 the root of studs, the concrete around studs would be crushed and cracked at a relatively high rate, while
 261 the ultimate capacity would also be soon reached. As reflected on the load-slip curves in Figs. 6b and
 262 d, the capacity decreases with a very steep slope after the ultimate load.

263 *2.3.3 Comparison with test data from the literature*

264 For a better understanding of the shear performance of PCSS connectors, further data analysis has
 265 been performed on a list of typical push-out test results available from the literature [27]-[34]. Since the
 266 PCSS specimen shows a notable difference in the ultimate capacity and the slip of the descending stage,
 267 the two indicators have been used in the comparison. It is worth stating that the flat concrete deck was
 268 employed in all the investigated push-out tests. The results are visualised in Fig. 9.



269 Fig. 9. Comparison between the reference and present test data: (a) Ultimate capacity; (b) slip of the
 270 descending stage.

271 For better comparison, the measured capacity per stud N_v^t has been normalised by dividing the
272 nominal capacity, i.e., the strength f_{std} multiple the sectional area A_{std} . Besides, the regression line is
273 also derived and included in Fig. 9a, including the mean and the two-sided 97.7% tolerance interval. In
274 the CSS specimen VS3 and VS4, the value falls below the mean and around the lower limit, indicating
275 a lower capacity per studs compared with the flat specimen. On the contrary, the value of PCSS
276 specimen HS3 and HS4 distributed between the mean and the upper limit, suggesting a higher capacity
277 in the PCSS specimen. Above all, the PCSS connector is proven to offer a satisfying capacity along
278 with the enhanced feasibility in prefabricating.

279 According to Chen and Kunitomo [35], the flexibility is determined by the ratio of the stud height
280 to diameter, i.e., h/d . To this end, the slip of the descending stage S_d is plotted against the ratio h/d , as
281 shown in Fig. 9b. Similarly, the regression lines are derived and plotted, including the mean and the
282 two-sided 97.7% tolerance interval. Except for the test data of VS4 specimens, the measured values are
283 well above the upper tolerance limit. Meanwhile, the PCSS specimens HS3 and HS4 show a notably
284 higher slip S_d compared with the CSS specimens and reference data. As a result, a better ductility and
285 capacity at the descending stage can be achieved by using the PCSS connector.

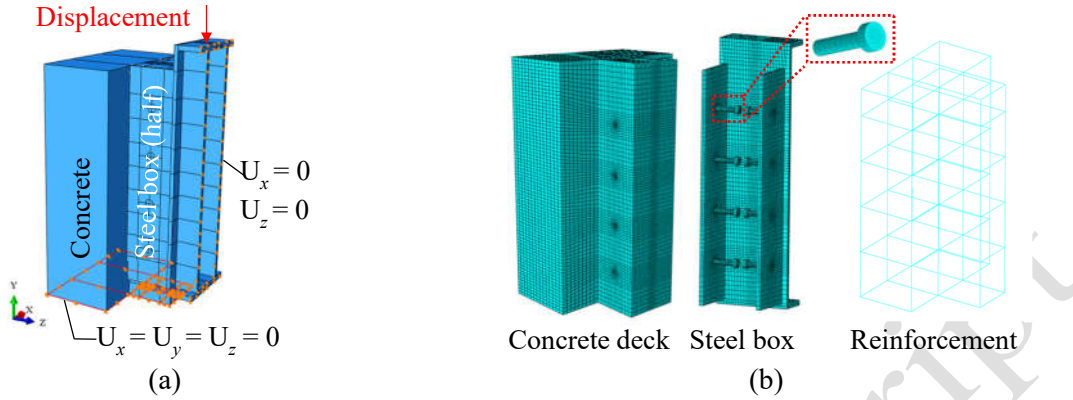
286 In terms of the failure model, the traditional specimen is highly similar to the CSS specimen. The
287 failure is mainly induced by the cutting of studs, while cracks initiated in the concrete around the studs
288 and then propagated to visible size when failed. On the contrary, the PCSS specimen demonstrates a
289 notably different failure model, i.e., only the concrete in the vicinity of the studs has been partly crushed
290 with moderate cracks after failed. As a result, a significant plateau could be observed from the
291 corresponding load-slip curves, as shown in Figs. 6a and c.

292 **2.4 Investigation on load transfer mechanism of PCSS specimens**

293 *2.4.1 Finite element model*

294 For a better understanding of the load-transfer mechanism of PCSS connectors, a high-resolution
295 finite element (FE) model of the specimen HS4 has been established using the commercial software
296 Abaqus [36], as shown in Fig. 10. In order to downscale the solution cost, the symmetry is utilised so
297 that only half the specimen is modelled. The 3D solid element C3D8R [36] is employed with the

298 adaptive meshing to balance accuracy and efficiency. The element size is defined as 2 mm in the 50×50
 299 mm region around studs and then gradually increase to 10 mm outside the region.



300 **Fig. 10.** FE model of HS4: (a) modelling and boundary condition; (b) element and meshing.

301 The concrete and steel are connected via the “hard contact” algorithm [37], i.e., only the
 302 compressive contact force and friction are allowed on the contact surface. In addition, the friction
 303 coefficient between concrete and steel is set to 0.6. The loading has been simulated via displacement,
 304 of which the maximum is set as 6 mm after the test. Since the FE model includes the complicated
 305 nonlinearity in both the material, geometry and contact, the dynamic solver Abaqus/Explicit [38] has
 306 been used to keep the solution intractable. Trial calculations have been performed with various loading
 307 rates, and the optimal value has been found around 0.6 mm/s, which balances accuracy and efficiency.

308 2.4.2 Material properties

309 In simulating material properties of the concrete deck, the concrete damage plasticity (CDP) model
 310 is employed as per the suggestion by Nie and Wang [39]. Another crucial aspect of the material model
 311 is the uniaxial stress-strain curve, including the compressive and tensile parts. In the compressive part,
 312 the empirical equation proposed by Guo [40] has been used, as shown in Equations 2a and b.

$$313 \quad y = \begin{cases} a_1 x + (3 - 2a_1)x^2 + (a_1 - 2)x^3, & 0 \leq x \leq 1 \\ \frac{x}{a_2(x-1)^2 + x}, & x \geq 1 \end{cases} \quad (2a)$$

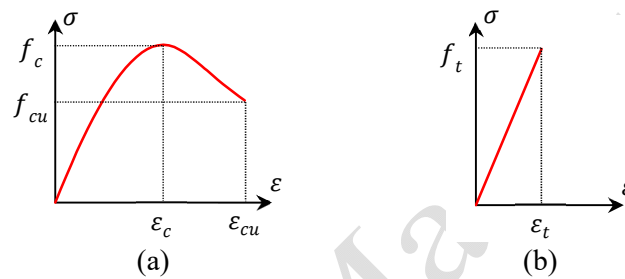
$$314 \quad y = \sigma/f_c \quad , \quad x = \varepsilon/\varepsilon_c \quad (2b)$$

315 Where σ and ε stand for the stress and strain, respectively; a_1 is the slope factor for the ascending stage,
 316 which is set as 1.7 as per [40]; a_2 is the slope factor for the descending stage, which is set as 2.0 as per
 317 [40]; f_c is the uniaxial compressive strength, respectively; ε_c is the reference strain at the peak stress,
 318 set as 0.002 according to [40].

319 The cubic strength f_{cube} is determined from the material test as shown in Table 2, while the
 320 uniaxial strength f_c is determined as $0.76f_{cube}$ [41]. Meanwhile, the maximum compressive strain is
 321 determined as 0.0035 [40]. Besides, the Poisson's ratio of the concrete is determined as 0.2 [41]. In the
 322 tensile part, the linear simplification [42] has been used, i.e., the stress increases proportionally with the
 323 strain until the ultimate tensile strength f_t is reached. After that, the stress is released from the cracked
 324 concrete and re-distributed to the nearby part. According to [41], the uniaxial tensile strength f_t could
 325 be derived based on the cubic compressive strength f_{cube} , as shown in Equation 3.

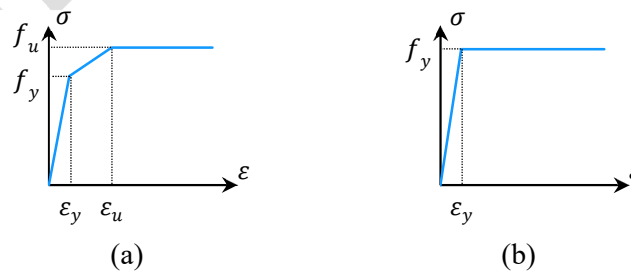
$$326 \quad f_t = 0.395f_{cube}^{0.55} \quad (3)$$

327 Thus, the uniaxial strain-stress relation of the concrete is derived, as shown in Figs. 11a and b.



328 **Fig. 11.** Uniaxial stress-strain curve of the concrete: (a) Compression; (b) Tension.

329 In the case of the steel, the trilinear model with hardening is applied to steel studs, as shown in Fig.
 330 12a, including the yielding strength f_y and strain ϵ_y , and the ultimate strength f_u and strain ϵ_u .
 331 Meanwhile, the bilinear model is used for the steel box and reinforcement, as shown in Fig. 12b, with
 332 the properties f_y and ϵ_y only. Besides, the Poisson's ratio of the steel is set to 0.3 according to [43].

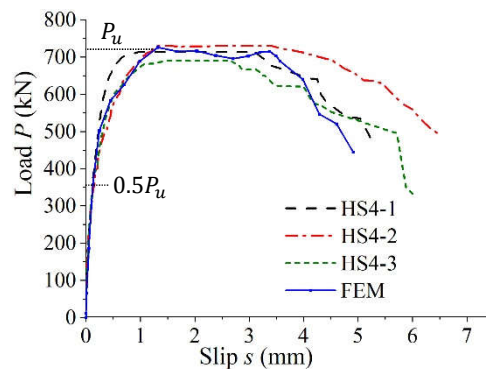


333 **Fig. 12.** Constitutive model of the steel: (a) Trilinear; (b) Bilinear.

334 2.4.3 Numerical results and discussion

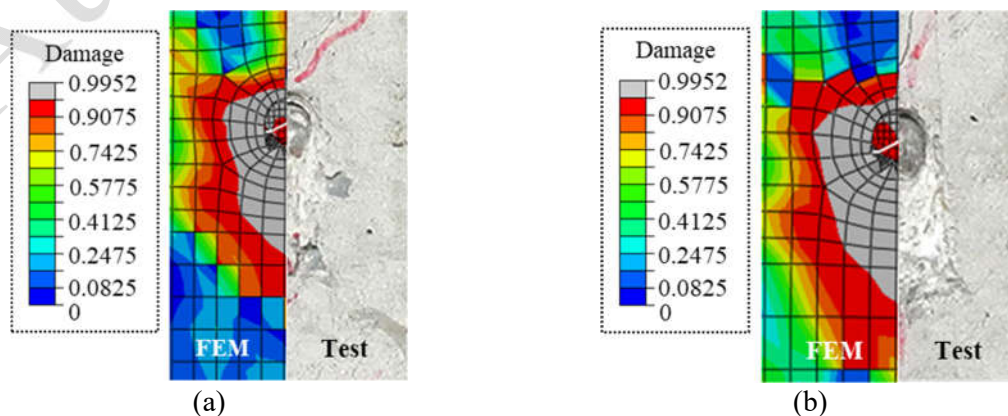
335 The predicted load-slip curve calculated from the FE model is shown in Fig. 12, combined with
 336 the test curves. Overall, the FE result is in good agreement with the test data. In the elastic stage when
 337 $P < 0.5P_u$, the slip increases proportionally with the load while little discrepancy could be found

338 between the FEM and test, i.e., no more than 4.7%. As the load increase beyond 50% of the peak load,
 339 a slight discrepancy occurs between the FE prediction and test result. As the loading continues, the FE
 340 model reached its ultimate capacity of 725 kN, which is 2.0% higher than the measured mean capacity
 341 of 711 kN. Meanwhile, the predicted slip at the peak load is 1.32 mm, i.e., about 15% higher than the
 342 measured mean. Besides, a high similarity could also be found in the slip of plateau S_f , which is 2.05
 343 mm from test and 2.08 mm by the FE (only 1.4% difference). After that, the slip increases while the
 344 load keeps decreasing, i.e., the descending stage. Finally, the FE model failed at the load of 420 kN due
 345 to convergence difficulties. A visible difference can be found between the FE and test curves, but the
 346 trend is still highly similar.



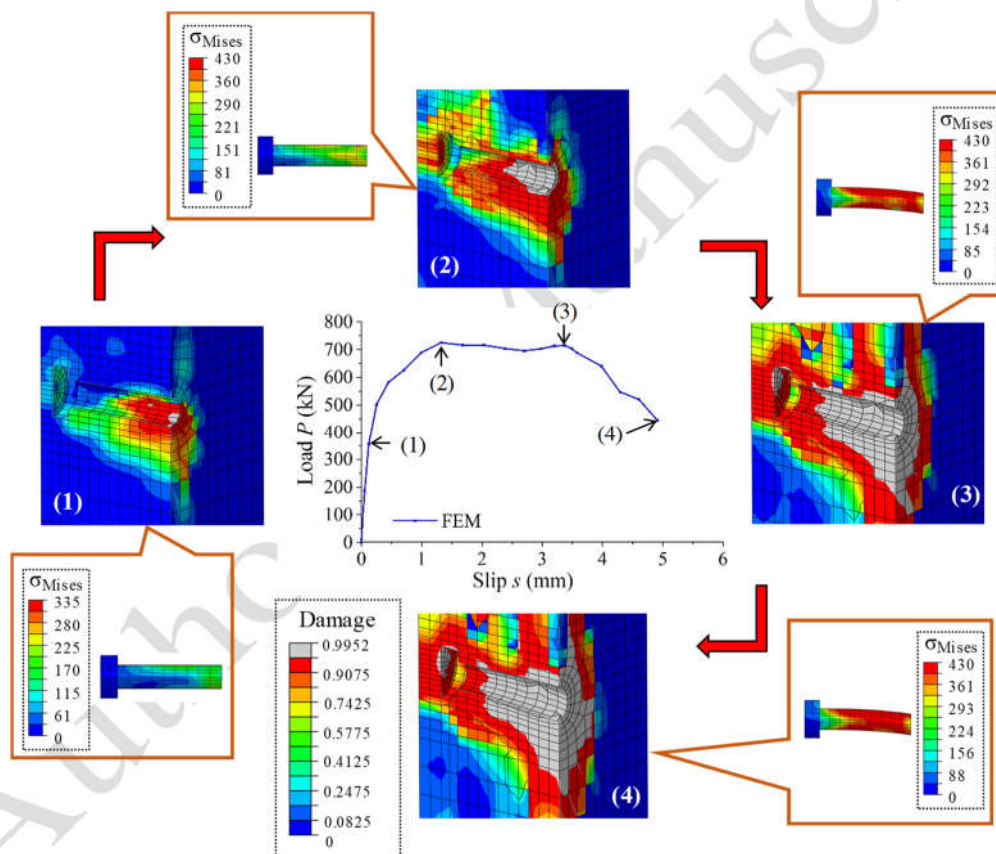
347
 348 **Fig. 13.** Comparison of load-slip curves between test and FE model

349 Further comparison is carried out on the crushing state of concretes at the failure state between the
 350 FE model and the specimen HS4-2, as shown in Figs. 14a and b. The FE results are presented in terms
 351 of damage factor indicating the crushing state of concretes. The comparison also suggests a good match
 352 in the failure state between the test and FE prediction. Thus, the established FE model is able to reflect
 353 the behaviour of the push-out tests.



354 **Fig. 14.** Comparison of concrete crushing between HS4-2 and FE model: (a) Concrete near the 2nd
 355 row of studs; (b) oncrete near the 3rd row of studs.

356 Based on the verified FE model, the load transfer mechanism in the PCSS is investigated in terms
 357 of damage in the concrete and Von Mises stress in the stud, as shown in Fig. 15. Generally, the loading
 358 process can be divided into 4 phases by 4 points on the load-slip curve. Before loaded to 363 kN (about
 359 50% the peak load), the specimen demonstrates almost perfectly linear behaviour on the load-slip curve.
 360 Accordingly, no obvious damage could be identified at the concrete, and the stud stress is well below
 361 the yield strength. Once loaded to 363 kN (about 50% the peak load), the concrete damage starts to
 362 initiate near the root of studs, as shown by the grey part in Point (1). Meanwhile, the maximum stud
 363 stress reaches 335 MPa, very close to the yield strength of 340 MPa. However, the interaction between
 364 the stud and concrete is still fully active due to the very limited concrete damage.



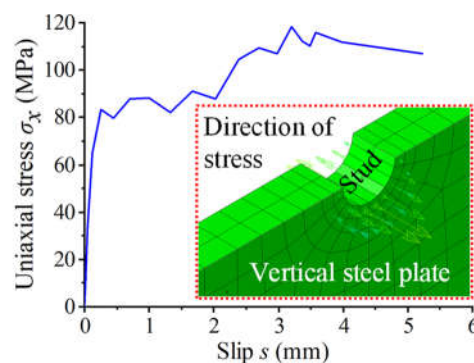
365
 366 **Fig. 15.** Evaluation of concrete damage and stud stress during the loading.

367 With further loading, the proportion of crushed concrete increases, and the studs gradually begin
 368 yielding. As a result, notable nonlinearity can be observed on the load-slip curve. Once loaded to the
 369 peak value of 725 kN, as shown by Point (2), the crushed concrete becomes interconnected around the
 370 hole. However, the diameter of the crushed region is only about 1.5 mm. Moreover, a small part of studs
 371 reaches the yielding and even ultimate strength. In general, although the stud yielding and concrete

372 crushing occur in the PCSS specimen at this stage, a good interaction still exists between the stud and
373 concrete. This is highly similar to the traditional stud connector. As a result, the PCSS connector
374 behaves like the traditional stud before the peak load.

375 After that, the load-slip curve shows a plateau until Point (3). Between Points (2) and (3), the slip
376 increases by almost 171%, while the crushed concrete region extends from 1.5mm to 4.5 mm in
377 diameter. Besides, most part of the stud reaches the ultimate strength at Point (3). The notable plateau
378 can be attributed to the lateral constraint on the concrete by the two vertical steel plates. With the
379 constraint, both the ultimate strength and ductility are enhanced for the concrete within the plates. Thus,
380 the stud-concrete interaction still lasts for a notable time period even after the ultimate of studs has been
381 achieved. As a result, the remarkable plateau can be observed on the load-slip curve before the final
382 fracture of studs. After Point (3), most part of the stud reaches the ultimate strength. Thus, the load
383 capacity of the specimen degrades, reflected by the descending load-slip curve. However, it is very
384 interesting that the volume of crushed concrete stays almost stationary until the failure. This could be
385 attributed to the lateral constraint on the concrete offered by the vertical steel plate. Thus, the specimen
386 still shows a considerable remnant capacity during the descending stage.

387 In order to further explore the lateral constraint effect on the concrete, the out-of-plane normal
388 stress has been derived for the vertical plate near the stud, as shown in Figs. 16. According to the result,
389 inter-extrusion between the concrete and vertical steel plate, and the stress increase with the slip until
390 the final failure. As a result, the lateral deformation of the concrete is constrained by the vertical steel
391 plate, which in turn help to control the proportion of crushed concretes around studs. As a result, a
392 notable slip could be observed in the descending stage of the load-slip curve.



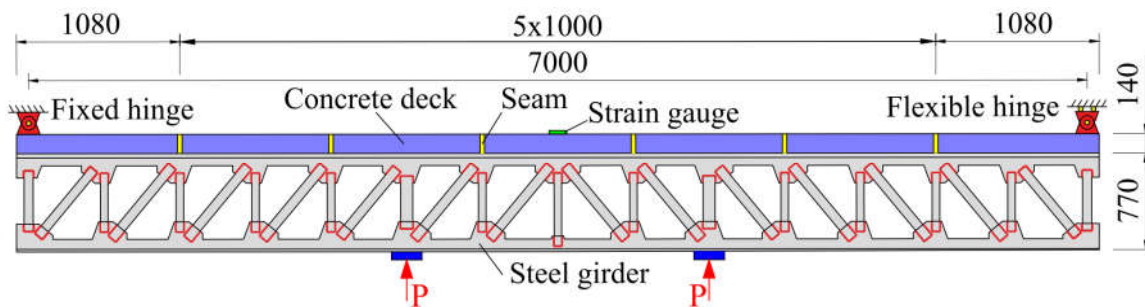
393
394

Fig. 16. Out-of-plane normal stress of the vertical steel plate near studs.

395 **3. Investigation on the prefabricated composite bridges using the PCSS**

396 **3.1 Full-scale model test of the composite bridge using PCSS**

397 A full-scale model test of the prefabricated steel-concrete composite bridge has been employed to
398 investigate the mechanical behaviour of prefabricated composite bridges using the PCSS, as shown in
399 Figs. 17 and b.



400 (a)



401 (b)

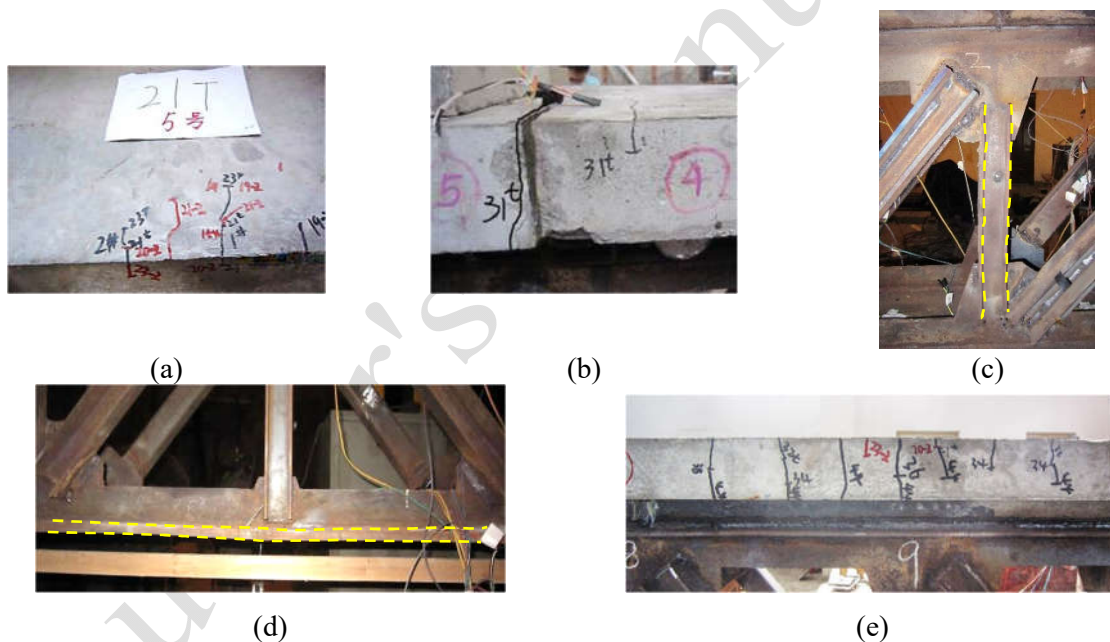
402 **Fig. 17.** Full-scale test of the prefabricated composite specimen: (a) Elevational view (Unit: mm); (b)
403 Photograph.

404 The specimen consists of a steel truss girder and a pre-cast concrete deck prestressed by tendons.
405 The PCSS connector has been employed to connect the deck and the top flange of the upper chords in
406 the truss. The specimen is simply supported with a span of 7000 mm. Two actuators working in-phase
407 have been used to load the specimen from bottom-up, through which the negative bending moment is
408 simulated. Meanwhile, a strain gauge is installed on the top surface of the concrete at the mid-span, as
409 shown in Fig. 17a.

410 The materials used in the full-scale test have been kept the same as those employed in the previous
411 push-out test, as listed in Table 2. Besides, the prestress is applied on the deck through the steel tendon
412 $1\phi^{s}15.2-1860$ [25], of which the ultimate strength is 1860 MPa. In the prefabrication, the deck has been
413 divided into 7 blocks, each of which is 1000 mm in length. The PCSS connector is embedded in the
414 deck blocks when casting, with a total of 28 studs in a single block. After that, the deck blocks with the
415 PCSS embedded are integrated through preloading the steel tendons. The Grade-A binder [44] has been
416
417

418 injected into the seams between deck blocks before applying the prestress to improve the integrity of
 419 the deck. The elastic modulus of the binder is 3200 MPa. Its tensile and compressive strengths are 8.5
 420 and 50 MPa, respectively. More details about the binder can be found from the reference [44].

421 Before loading, the tendons are preloaded to 1395 MPa from the two ends using the hydraulic
 422 jacks. Three hours after the preloading, the top-surface strain of the deck has been measured via the
 423 gauge shown in Fig. 17a, which is $-650 \mu\epsilon$. Three loading phases have been conducted on the specimen
 424 during the test, and the results are illustrated in Figs. 18a to e. In the first phase, the specimen is loaded
 425 and unloaded for three cycles under the load of $P = 180 \text{ kN}$. Overall, the specimen demonstrates the
 426 elastic behaviour, and no apparent crack has been found. Also, the strain on the top surface of the deck
 427 is measured as $-182 \mu\epsilon$, indicating enough remnant prestress and compressive state of the deck. As a
 428 result, the deformation and stress increase and decrease linearly with loading and unloading.



429 **Fig. 18.** Test result of the prefabricated composite specimen: (a) The first crack at the deck viewed
 430 from top; (b) The first crack at the seam viewed from elevation; (c) buckling of the vertical member
 431 near the bearing; (d) buckling of the lower chord at the midspan; (e) the longitudinal welded joint at
 432 the failure stage.

433 In the second phase, the specimen is at first loaded to $P = 210 \text{ kN}$. At the same time, the top-surface
 434 strain becomes $18 \mu\epsilon$, suggesting the prestress is completely eliminated by the external load. Thus, two
 435 cracks have been soon observed at the top surface of the deck near the loading site, as shown in Fig.
 436 18a, including the 1st crack marked as “1#” and the 2nd crack marked as “2#”. However, crack closure
 437 occurred at the observed cracking site directly after unloading.

438 At the third phase, the specimen is directly loaded until failure and the peak load attained is
439 recorded as the ultimate load, i.e., $P = 500$ kN. As the load increases to 310 kN, the first crack at the
440 seam has been observed, as shown in Fig. 18b. After that, cracks extensively initiate at the seams and
441 propagate much faster than the cracks within blocks. Finally, when the load increases to 500 kN,
442 buckling can be found at the vertical member, as shown in Fig. 18c, and the lower chord, as shown in
443 Fig. 18d. At the same time, the three deck blocks near the midspan are seriously cracked and split. Since
444 the load could not be increased anymore, the failure of the specimen is identified at the ultimate load of
445 500 kN, and the test is stopped. It is worth noting that the longitudinal welded joint between the PCSS
446 and truss has stayed intact during the whole loading process. As shown in Fig. 18e, no visible damage
447 could be found in the longitudinal welded joint when the failure of the specimen has occurred. On this
448 end, the feasibility is further verified for the longitudinal welded joint of PCSS connectors in
449 prefabricated composite bridges.

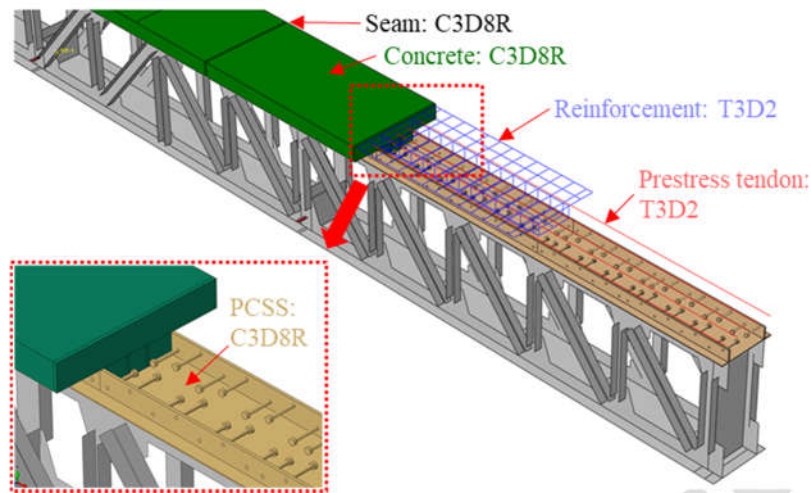
450 **3.2 Establishment of the numerical model**

451 *3.2.1 Element and meshing*

452 An advanced finite element (FE) model has been established for the full-scale prefabricated
453 composite specimen using the software Abaqus [36], as shown in Fig. 19. The concrete deck and PCSS
454 connectors are modelled with the solid element C3D8R, while the truss element T3D2 is used to
455 simulate the prestress tendons and reinforcements. In the steel truss girder, the structural members are
456 modelled with the shell element S4R. In the full-scale test, the binder was used to connect the deck
457 blocks at the seam. Since the binder's tensile strength (8.5 MPa) is favoured to the capacity, it is not
458 explicitly modelled. Instead, the seam is simulated by a 10 mm-wide concrete segment without
459 reinforcement for conservativeness.

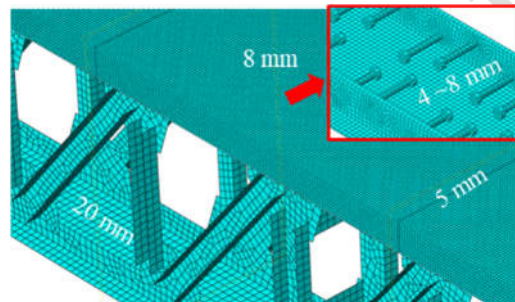
460 The details of element selection are also included in Fig. 19. Different meshing sizes have been
461 employed for the various components to ensure both the accuracy and computational feasibility, as
462 shown in Fig. 20. A relatively coarse meshing size is used for the shell elements simulating the steel
463 truss girder, i.e. 20 mm since it is not of special interest. The deck is modelled by the C3D8R with a
464 size of 8 mm. Accordingly, the PCSS connectors are discretized with a refined meshing size ranging
465 from 4 mm to 8 mm. For the seams between blocks, the meshing size of 5 mm is used to ensure the

466 sufficient layer of solid elements. A coarse meshing size, i.e. 37 mm, has been applied in modelling the
467 prestress tendons and reinforcements since they are mainly used to integrate the deck.



468
469

Fig. 19. Advanced FE model of the prefabricated composite specimen.



470
471

Fig. 20. Meshing of the advanced FE model.

472 3.2.2 Contact relation, boundary condition and material models

473 The deck is connected with the prestress tendons and reinforcements using the “embedding” hard
474 contact [36], i.e. the displacement-interpolation. Meanwhile, the welded joint between the top surface
475 of the truss and the vertical plates of PCSS connectors are modelled through the “tie” contact [36], i.e.
476 the displacement-coupling. Between the concrete and studs, the face-to-face hard contact has been
477 applied, and the friction coefficient is set as 0.6 according to [37].

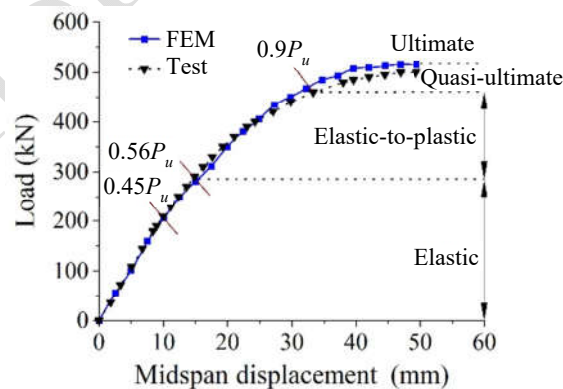
478 The boundary conditions of the FE model are set in accordance with the actual situation of the
479 prefabricated composite specimen shown in Fig. 17. The loading procedure has been simulated through
480 imposing a total displacement of 50 mm. Similarly, the solution has been carried out through the quasi-
481 static analysis using the Abaqus/Explicit dynamic solver to ensure computational efficiency. At first,
482 an artificial duration of 50 seconds is adopted for loading to failure, and the loading rate is accordingly

483 determined as 1 mm/second. After that, the adjustment is made to balance the efficiency and accuracy
484 through trial computations, using the procedures illustrated in section 3.2.

485 The material properties and models employed in section 2.4 have been adopted in the FE
486 simulation of the full-scale specimen, including the stud, steel plates and concrete since the materials
487 in the full-scale test are kept the same as in the push-out test. Besides, the prestress tendon has been
488 regarded as the elastic material since the used steel wire has no clear yielding point, and it stayed intact
489 until the failure of the specimen.

490 3.3 Verification of the FE model

491 The load-deflection curves obtained from the test and the numerical simulation are compared in
492 Fig. 21. When the load is below 56% of the ultimate load, i.e. $0.56P_u$, the prefabricated composite
493 specimen mainly demonstrates the linear elastic behaviour, and the FE curve matches very well with
494 the measured curve. For instance, under the load of 250kN, the displacement measured at the mid-span
495 of the specimen is 12.33 mm, while the corresponding FE value is 12.50 mm, i.e., about 1% error. As
496 the load further increases beyond $0.56P_u$, the curve gradually shows the notable nonlinearity, indicating
497 the elastic-to-plastic behaviour of the specimen. After loaded to $0.9P_u$, the mid-span deflection of the
498 specimen is 38.03 mm, while the FE value is 34.69 mm, i.e., an error of 8.7%. However, this difference
499 is somehow acceptable, considering the complexity in modelling nonlinear behaviour.



500
501

Fig. 21. Load-displacement curve of the prefabricated composite specimen.

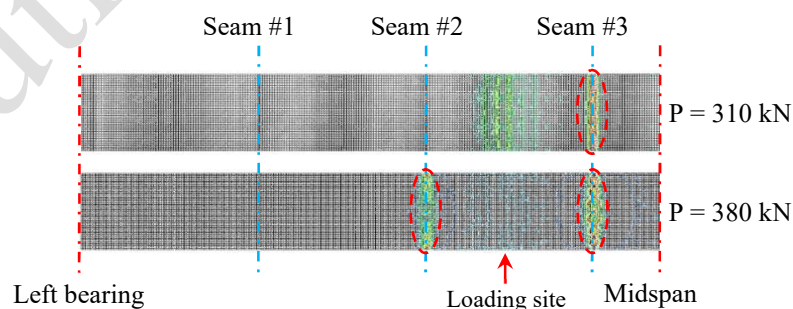
502 Overall, the derived load-deflection curve from FEM keeps in good agreement with test data.
503 Besides, the FE model also matches well with the test respecting the distribution of cracks and the
504 failure mode, which will be discussed in detail in the following section. To sum, the FE model is
505 validated by the test data.

506 3.4 Numerical Results

507 3.4.1 Classification of loading stages

508 As shown previously in Fig. 21, the mechanical behaviour of the prefabricated composite specimen
509 can be divided into three phases, including the elastic, elastic-to-plastic and quasi-ultimate stages. At
510 the elastic stage ($P < 0.56P_u$), the load-deflection curve shows a linear trend. As the load increased to
511 $0.45P_u$ (i.e., 210kN), notable tensile stress could be observed at several points on the deck top surface,
512 suggesting that the prestress is counterbalanced by the applied load. As a result, the first crack occurs
513 at the deck surface. However, the specimen still demonstrates elastic behaviour since the load and
514 deformation are almost in a linear relation.

515 At the elastic-to-plastic stage ($0.56P_u < P < 0.9P_u$), the prestress effect is entirely eliminated by
516 the load. In this situation, the deck works in the way of the reinforcement concrete (RC) member. As a
517 result, the load-displacement curve is no longer linear, but the change in slope is moderate. As the load
518 further increased to $0.62P_u$ (i.e., 310kN), the 1st cracking occurs at the seam close to the midspan, as
519 shown in Fig. 22. In RC members, the crack size would be directly controlled by the reinforcement
520 ratio. Since no reinforcement passes through the seam, the cracking-resistance becomes lower at the
521 seam compared with the pre-cast blocks. With the load further increasing to $0.76P_u$ (i.e., 380 kN), the
522 2nd cracking site appears at the seam near the midspan, as shown in Fig. 22. Along with the crack, an
523 abrupt change could be observed on the load-slip curve. At the quasi-ultimate stage ($P > 0.9P_u$), the
524 load-displacement curve gradually becomes flat, and the deformation increases rapidly with the load.



525

Fig. 22. Cracking site on the concrete deck

526

527 3.4.2 Stress and crack distribution at the ultimate stage

528 Figs. 23a and b respectively show the ultimate stress state and crack distribution from the FE model.
529 The result suggests that the yield stress is reached in a considerable proportion of the truss members,

530 especially in the web members and lower chords. Fig. 23b shows the distribution of cracks in the deck,
 531 in which the coloured parts indicate the cracked location. It can be found that cracks have already been
 532 fully developed in the three deck blocks near the midspan, similar to the cracks in the test specimen.
 533 Besides, the cracking at the seams between deck blocks is much more severe than that within the blocks.

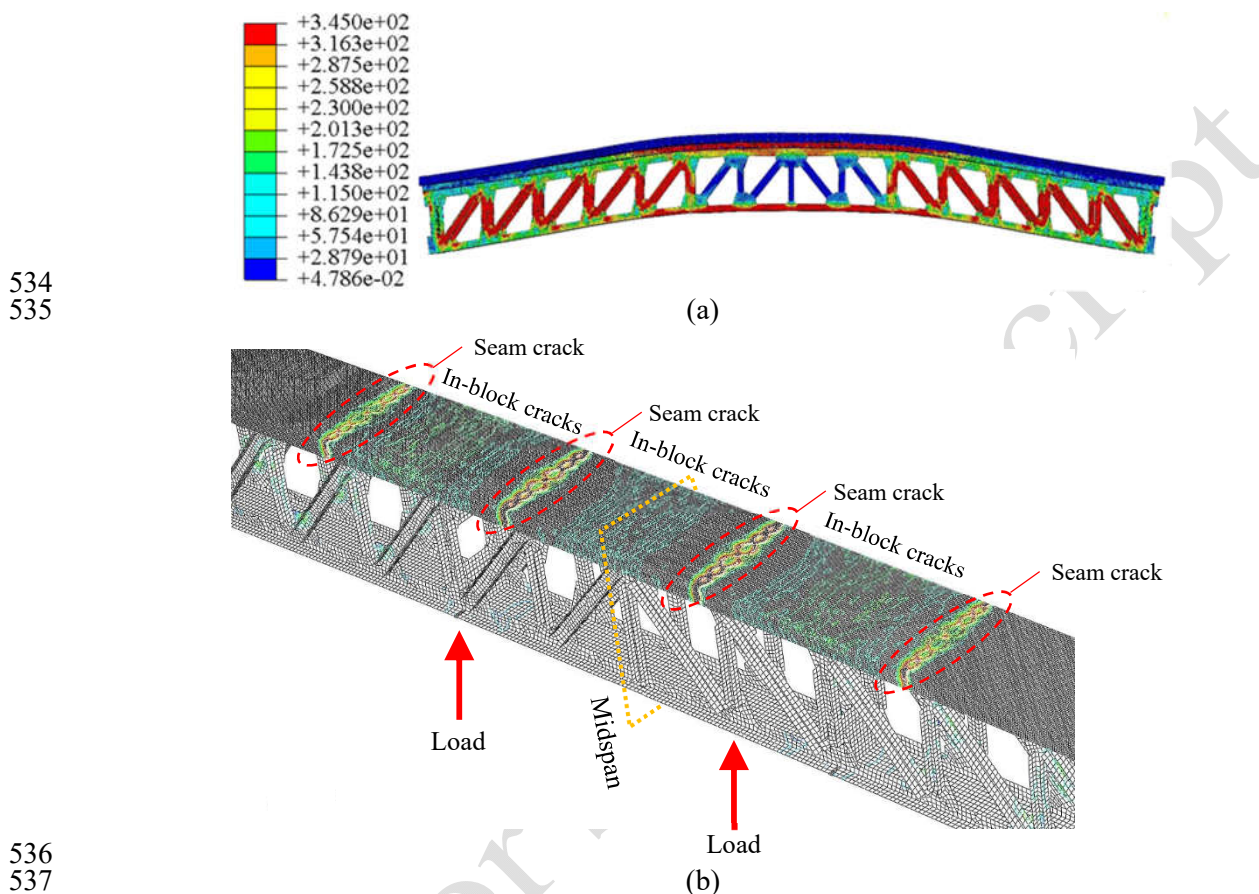
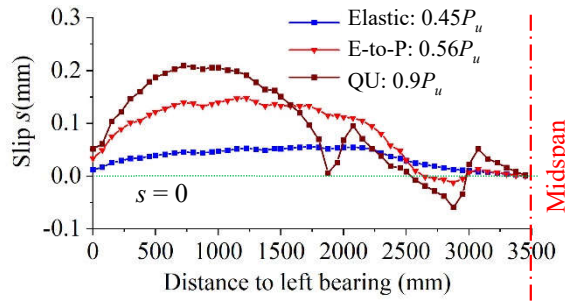


Fig. 23. FE result at the ultimate state: (a) Von Mises stress (MPa); (b) Crack distribution.

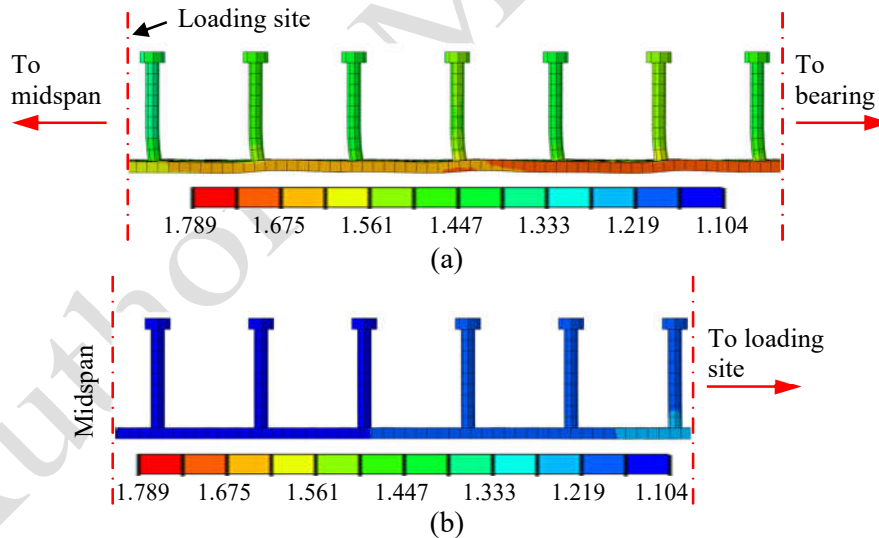
539 3.4.3 Distribution of slip at various stages

540 The slip between the deck and stud is calculated at the stud root, and the mean value from the studs
 541 with the same longitudinal position has been employed. Fig. 24 shows the representative distribution of
 542 the slip at three loading stages, including of the elastic stage, elastic-to-plastic (E-to-P) stage and quasi-
 543 ultimate (QU) stage. The result shows significant differences between the three stages. At the load of
 544 $0.45P_u$, i.e. the elastic stage, the slip is varied smoothly with the distance. Since the load increases to
 545 $0.56P_u$ at the E-to-P stage, the specimen demonstrates the elastic-to-plastic behaviour, and abrupt
 546 changes can be found in the distribution. After that, the abrupt change escalates with the increase in the
 547 load. As the load further grows to $0.9P_u$ at the quasi-ultimate stage, the abrupt changes become very
 548 remarkable, and sharp step changes can even be found at several points.



549
550 **Fig. 24.** Longitudinal distribution of the slip at different stages

551 During the elastic stage, the slip of PCSS connectors shows a continuous distribution, as shown
552 by the blue line in Fig. 24. The slip is relatively small at the bearing, and then gradually increases with
553 the distance until the loading point is reached. For better illustration, Figs. 25a and b show the
554 corresponding displacement of studs in the shear-bending zone and pure bending zone, respectively. In
555 the shear-bending zone, i.e. the zone from the bearing to the loading point, the displacement of studs
556 increases with the distance, as shown in Fig. 25a. In the pure bending zone between the two loading
557 points, symmetry trend can be observed. Especially, the displacement of studs gradually decreases to
558 zero from the loading point to the midspan, as shown in Fig. 25b.



559
560
561
562 **Fig. 25.** Displacement of studs at $0.45P_u$ (Unit: mm): (a) shear-bending zone; (b) pure bending zone.

564 When the load increase increases to $0.56P_u$, cracks initiate at the seam between deck blocks, as
565 shown in Fig. 26. As a result, the slip is no longer continuously distributed. Fig. 26 also includes the
566 displacement of studs near the seam crack, i.e. $l = 3000$ mm. The result suggests that the displacement
567 decreases to zero at the cracking site of the seam, and then symmetrically increases with the distance.
568 This effect can be related to the first zigzag in the slip shown in Fig. 26.

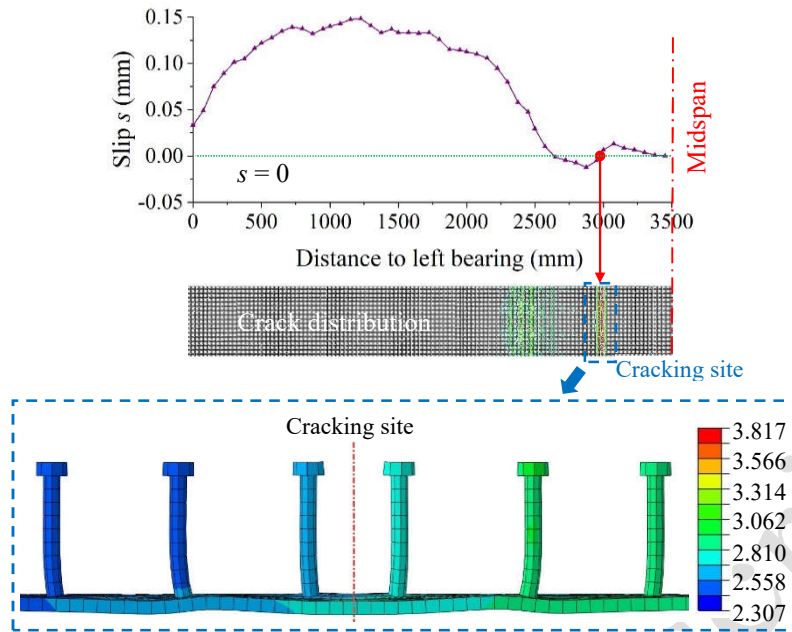


Fig. 26. Slip and stud displacement at $0.56P_u$ (Unit: mm).

569
570

571 As the load further increases beyond $0.56P_u$, the specimen demonstrates elastic-plastic behaviour,
572 and both the width and number of cracks continue to grow. Fig. 27 show the crack distribution and slip
573 at the load of $0.9P_u$. The result suggests the concentration of cracks in the three deck blocks near the
574 midspan, with the maximum cracking width at the seams. The slip of studs reduces to almost zero at
575 the two cracked seams near $l=1800$ mm and $l=3000$ mm, as shown in Fig. 27. Similarly, the abrupt
576 change can be observed at the two cracking sites in the slip, with an escalated scale.

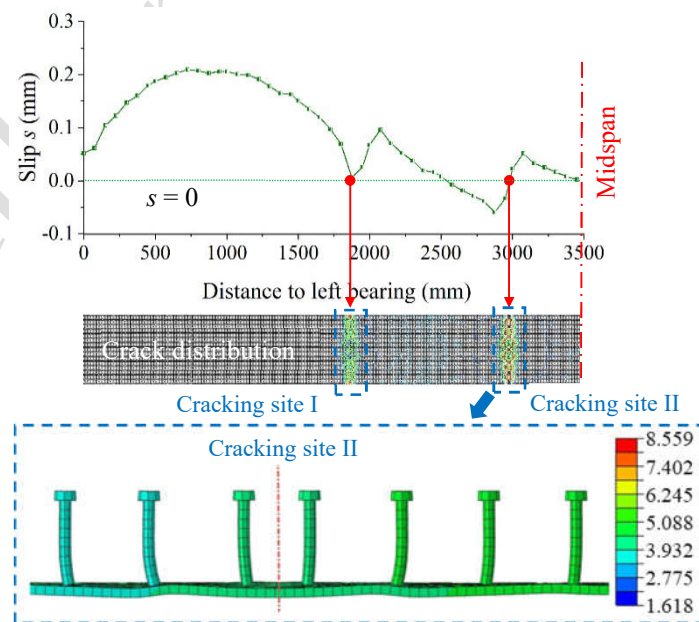
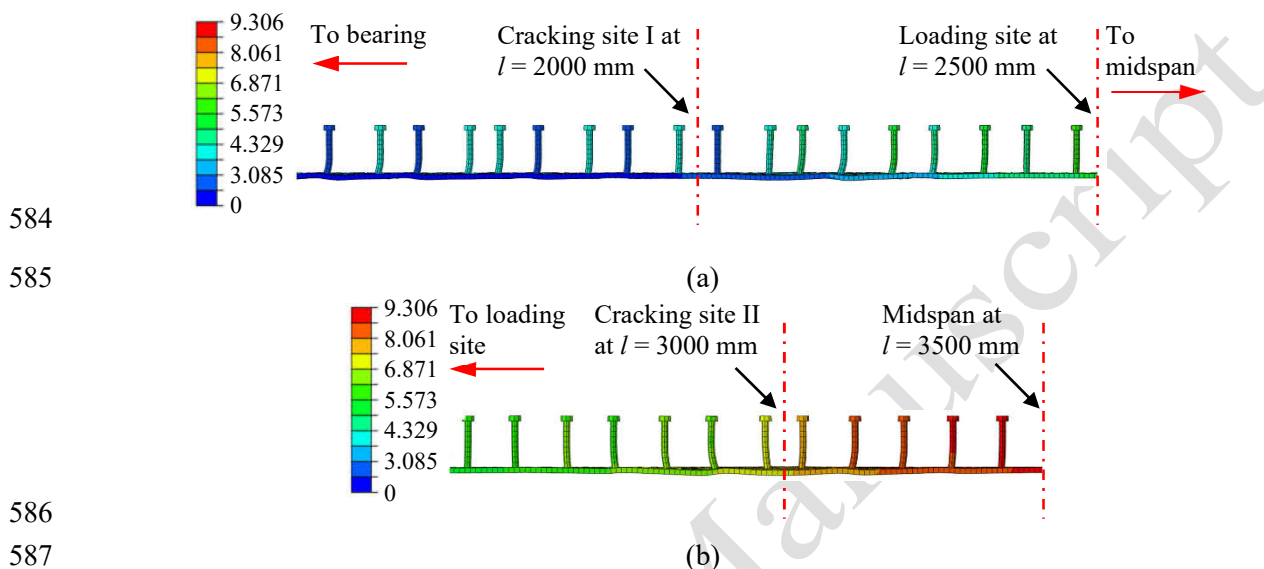


Fig. 27. Slip and displacement at $0.9P_u$ (Unit: mm).

577
578

579 When the load increase beyond 90% of the ultimate load, the cracks extensively develop, while
 580 the three decks in the midspan gradually cease to work. Meanwhile, the lower chord of the steel truss
 581 girder gradually yielded. At this stage, the abrupt increase can also be found in the slip of the studs near
 582 the cracked seams, as shown in Figs. 28a and b. Finally, the ultimate capacity is achieved since no
 583 additional load can be applied to the specimen.



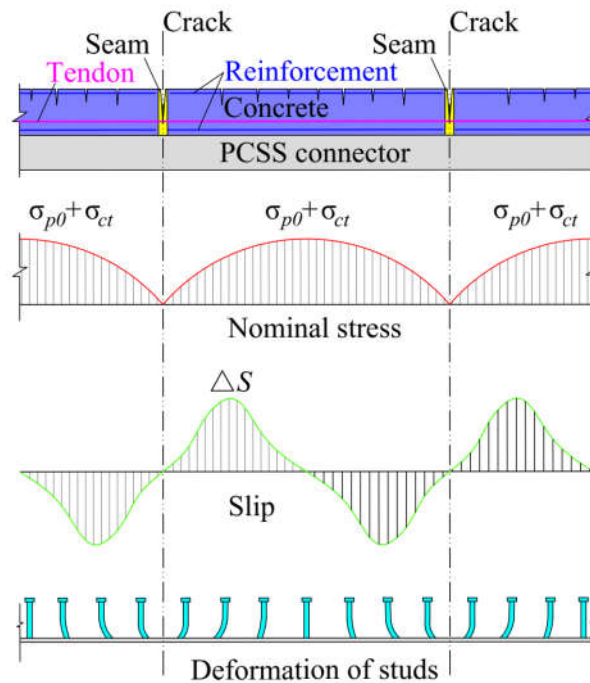
584
 585
 586
 587
 588 **Fig. 28.** Displacement of studs at the ultimate state (Unit: mm): (a) shear-bending zone; (b) pure
 589 bending zone.

590 3.5 Discussions on the numerical result

591 The slip distribution is also closely related to the configuration of the deck and the cracking feature
 592 of the prefabricated composite specimen. As described in section 3.1, once the crack initiates at the
 593 seam ($P = 310$ kN), it will develop at a much higher rate, and gradually become the major cause for the
 594 final failure of the specimen. This is mainly because the reinforcement is embedded within the deck
 595 blocks but no at the seam. Thus, the bond-slip theory [45] is used to illustrate the mechanism of shear-
 596 slip transfer between the concrete and steel, as shown in Fig. 29.

597 As the growth of cracks in the concrete, the stress at the cracked parts is gradually released from
 598 $\sigma_{p0} + \sigma_{ct}$ to 0, in which σ_{p0} is the prestress and σ_{ct} is the concrete stress. Accordingly, the released
 599 stress will be re-distributed to the nearby components, including the prestress tendons, truss members
 600 and uncracked concretes. The released stress increases from zero at the cracked seam to a peak value at
 601 a certain distance from the crack and then decreases to zero again with the distance. As a result of the
 602 stress redistribution, an additional slip Δs will be induced between the concrete and steel near the

603 cracked seam. Similar to the stress redistribution, the additional slip reaches its peak at a certain distance
 604 from the cracked seam and then falls back to zero with the distance. Consequently, the abrupt changes
 605 could be found in the distribution of slip along the girder.



606
 607 **Fig. 29.** Redistribution of stress and slip in the PCSS specimen after cracking at the seam.

608 4. Conclusions

609 In this paper, a series of experimental and numerical works have been carried out to investigate the
 610 load-slip behaviour of an innovative prefabricated shear stud (PCSS) connector and its application in
 611 the prefabricated steel-concrete composite bridges. The following conclusions can be drawn:

- 612 ● Push-out tests have been performed on a total of 12 specimens, including 6 PCSS specimens and 6
 613 specimens with the conventional shear stud (CSS). Overall, the ultimate capacity of the PCSS
 614 specimen is about 39.1%-67.3% higher than the CSS specimen. Meanwhile, the PCSS specimen
 615 shows the notable “flat plateau” and descending stage on the load-slip curve after the peak load,
 616 which ensures a much better ductility. Besides, the concrete was just slightly crushed near the stud
 617 root in PCSS specimens, compared with the well-developed cracks in the CSS specimens.
- 618 ● Comparison has also made between the test result and the data from the literature, in which the flat
 619 concrete deck was used, in terms of the capacity per studs and slip of descending stage. According
 620 to the result, the normalised stud capacity of the PCSS specimen falls between the mean value and

621 upper tolerance limit derived from the literature, further indicating a satisfying capacity of PCSS
622 specimens. Meanwhile, the slip of the descending stage in the PCSS specimen is well above the
623 upper limit by the literature, suggesting a better ductility. To sum, the PCSS connector enables the
624 full prefabrication of composite bridges without compromise in the capacity and ductility.

625 ● A high-resolution FE model has been established for the PCSS specimen and validated through the
626 test data. Based on the model, the investigation is performed to investigate the load transfer
627 mechanism of the PCSS connector at the component-level, including the stress of studs, damage of
628 concretes, and stress state of vertical steel plates. The result reveals that the ultimate capacity of the
629 PCSS is mainly controlled by the yielding of studs. However, the surrounding concrete could
630 provide an effective constraint on the studs after they yielded, leading to the notable plateau and
631 descending stage in the load-slip curve. At the same time, the damage of concretes is limited by the
632 lateral constraint from vertical steel plate, resulting in a remarkable improvement in ductility of the
633 PCSS specimen.

634 ● A full-scale model test is employed to verify the application of PCSS connectors in prefabricated
635 composite bridges. Based on the test, an advanced FE model has been established for the specimen
636 and validated using the test data. The result shows that the slip distribution is influenced by the
637 cracking at the seam between prefabricated deck blocks. As a result, the abrupt changes can be
638 found in the load slip curve after cracking occurs, which differs from the traditional composite
639 bridges.

640 **Acknowledgements**

641 The research is supported by the National Natural Science Foundation of China (Project No: 51778094),
642 the Natural Science Foundation of Chongqing City, China (Grant No. cstc2018jcyjAX0509,
643 cstc2020jcyj-msxm1602) and the Science and Technology Project of DOT of Yunnan Province, China
644 (Project No: 2018-28).

645 **Conflict of Interest**

646 There is no conflict of interest associated with this publication.

647 **Data Availability Statement**

648 All the data, model or code data employed in the study appear in the submitted paper.

649 **References**

- 650 [1] Johnson, R.P., Composite structures of steel and concrete: beams, slabs, columns, and frames
651 for buildings, 3rd edition, John Wiley & Sons, Hoboken, US, 2008.
- 652 [2] Hällmark, R., White, H., & Collin, P. (2012). Prefabricated bridge construction across Europe
653 and America, PRACT. PERIOD. STRUCT. DES. CONSTR., 17(3): 82-92.
654 [https://doi.org/10.1061/\(ASCE\)SC.1943-5576.0000116](https://doi.org/10.1061/(ASCE)SC.1943-5576.0000116)
- 655 [3] Chaudhary, S., Pendharkar, U., & Nagpal, A. (2009). Control of creep and shrinkage effects in
656 steel concrete composite bridges with precast decks, J. BRIDGE ENG., 14(5): 336–345.
657 [https://doi.org/10.1061/\(ASCE\)1084-0702\(2009\)14:5\(336\)](https://doi.org/10.1061/(ASCE)1084-0702(2009)14:5(336))
- 658 [4] Ehab, E., & Dennis, L. (2002). Modelling of headed stud in steel-precast composite beams,
659 STEEL COMPOS. STRUCT., 2, No. 5, 355-378. <https://doi.org/10.12989/scs.2002.2.5.355>
- 660 [5] Shim, C.S., Chung, C.H., Kim, I.K., & Kim, Y.J. (2010). Development and Application of
661 Precast Slabs for Composite Bridges, STRUCT. ENG. INT., 20(2): 126-133.
662 <https://doi.org/10.2749/101686610791283623>
- 663 [6] Huang, D., Wei, J., Liu, X., Xiang P., & Zhang, S. (2019). Experimental study on long-term
664 performance of steel-concrete composite bridge with an assembled concrete deck, CONSTR
665 BUILD. MATER., 214: 606–618. <https://doi.org/10.1016/j.conbuildmat.2019.04.167>
- 666 [7] Nijgh, M. P., Gîrbacea, I. A., & Veljkovic, M. (2019). Elastic behaviour of a tapered steel-
667 concrete composite beam optimized for reuse, ENG. STRUCT., 183: 366–374.
668 <https://doi.org/10.1016/j.engstruct.2019.01.022>
- 669 [8] Mirza, O., Kaewunruen, S., Kwokand, K., & Griffin, D.W.P. (2016). Design and modelling of
670 pre-cast steel-concrete composites for resilient railway track slabs, STEEL COMPOS.,
671 STRUCT., 22(3): 537-565. <https://doi.org/10.1016/j.istruc.2019.03.006>
- 672 [9] Shim, C S., Jeon, S.M., & Kim, D.W. (2008). Evaluation of static strength of group stud shear
673 connection in precast concrete deck bridges, BRIT. MED. J., 20(2): 672-684.

- 674 [10] Xiang, Y., GUO, S., Zheng, Q., Chen, Z., & Lin, H. (2017). Influence of Group Studs Layout
675 Style on Static Behavior of Steel-Concrete Composite Small Box Girder Models, J. BUILD.
676 STRUCT., 38(s1):376-383. <https://doi.org/10.14006/j.jzjgxb.2017.S1.053>
- 677 [11] Wang, Y., Yu, J., Liu, J., & Frank, Y. (2019). Shear behavior of shear stud groups in precast
678 concrete decks, ENG. STRUC., 187: 73–84. <https://doi.org/10.1016/j.engstruct.2019.02.002>
- 679 [12] Sjaarda, M., Porter, T., West, J.S., & Walbridge, S. (2017). Fatigue Behavior of Welded Shear
680 Studs in Precast Composite Beams. J. BRIDGE ENG., 22(11): 04017089.
681 [https://doi.org/10.1061/\(ASCE\)BE.1943-5592.0001134](https://doi.org/10.1061/(ASCE)BE.1943-5592.0001134).
- 682 [13] Liu, M., Wan, J., & Zhang, Q. (2014). Mechanical Analysis of a Steel-concrete Composite
683 Girder Bridge under Cluster Distribution and Uniform Distribution of the Shear Studs, J. CIVIL
684 ENG. MANAG., 31(3):1-6. <https://doi.org/10.13579/j.cnki.2095-0985.2014.03.020>
- 685 [14] Papastergiou, D., & Lebet, J.P. (2014). Design and Experimental Verification of an Innovative
686 Steel-Concrete Composite Beam, J. CONSTR. STEEL RES., 93, 9-19.
687 <http://dx.doi.org/10.1016/j.jcsr.2013.10.017>
- 688 [15] FHWA. Connection details for prefabricated bridge elements and systems, FHWA-IF-09-010,
689 office of engineering., bridge division, Washington, DC, US, 2009.
- 690 [16] Ahmed S., & Karavasilis, T. (2018). Removable shear connector for steel-concrete composite
691 bridges, STEEL COMPOS. STRUCT., 29. 107-123.
692 <http://dx.doi.org/10.12989/scs.2018.29.1.107>
- 693 [17] Su, Q., & Li Y. (2015). Shear capacity of grouped stud connector embedded by high strength
694 mortar, J. TONGJI UNI. (natural science), 43(5):699-705. (in Chinese)
695 <http://dx.doi.org/10.11908/j.issn.0253-374x.2015.05.008>
- 696 [18] Balkos, K.D., Sjaarda, M., West, J.S., & Walbridge, S. (2019). Static and fatigue tests of steel-
697 precast composite beam specimens with through-bolt shear connectors, J. BRIDGE ENG.,
698 24(5): 04019036. [http://dx.doi.org/10.1061/\(ASCE\)BE.1943-5592.0001382](http://dx.doi.org/10.1061/(ASCE)BE.1943-5592.0001382).

- 699 [19] Chen, Y.T., Zhao, Y., West, J.S., & Walbridge, S. (2014). Behavior of steel–precast composite
700 girders with through-bolt shear connectors under static loading, *J. CONSTR. STEEL RES.*, 103
701 168–178. <http://dx.doi.org/10.1016/j.jcsr.2014.09.001>
- 702 [20] Liu, X., Bradford, M. A., & Ataei, A. (2017). Flexural performance of innovative sustainable
703 composite steel-concrete beams, *ENG. STRUCT.*, 130:282-296.
704 <http://dx.doi.org/10.1016/j.engstruct.2016.10.009>
- 705 [21] Zhou, Z.X. (2012). Prestressed steel- concrete composite continuous rigid frame bridge and
706 construction: China, ZL 200910104675. X, Patent Office of China. (in Chinese)
- 707 [22] Zhou, Z.X. (2014), the Shear Connectors of PCSS: Germany, PCT/CN2014/075541. German
708 Patent Office. (in German)
- 709 [23] Gao, Y.M., Zhou, Z.X., Liu, D., & Wang Y. (2016). Cracking of a prefabricated steel truss-
710 concrete composite beam with pre-embedded shear studs under hogging moment, *STEEL*
711 *COMPOS. STRUCT.*, 5: 981-997. <http://dx.doi.org/10.12989/scs.2016.21.5.981>
- 712 [24] MHURD of China. Code for design of steel and concrete composite bridges (GB 50917-2013),
713 JHPRESS, Beijing, China, 2013. (in Chinese)
- 714 [25] MOT of China. Specifications for design of highway reinforced concrete and prestressed
715 concrete bridges and culverts (JTG 3362-2018), CCPRESS, Beijing, China, 2018. (in Chinese)
- 716 [26] Oehlers, D.J., & Bradford M. (1999). Elementary Behaviour of Composite Steel and Concrete
717 Structural Members, Butterworth-Heinemann [J], 1999: 21-38.
- 718 [27] Chen, Y., Lu, P., Song, X., & Liu, Y. (2012). Test Study of Shear Performance of Shear Studs
719 for Steel-Concrete Composite Beams. *Bridge Construction*, 42(3): 63-69.
- 720 [28] Zhong, Q. (2017). The experimental study on composite steel-prefabricated precast concrete
721 slab beam. Hunan University.
- 722 [29] Xue, W., Ding, M., Wang, H., & Luo, Z. (2009). Experimental studies on behavior of stud
723 shear connectors under monotonic loads. *30 (1): 95-100.*
- 724 [30] Zhang, J., Hu, X., Fu, W., Du, H., Sun, Q., & Zhang, Q. Experimental and theoretical study on
725 longitudinal shear behavior of steel-concrete composite beams, *J. CONSTR. STEEL*
726 *RES.*,171:1-18. <http://10.1016/j.jcsr.2020.106144>

- 727 [31] Luo, Y. (2008). Research on shear Connectors of Steel-concrete composite Beams. Central
728 South University.
- 729 [32] Oehlers, D.J., & Park, S.M. (1992). Shear Connectors in Composite Beams with Longitudinally
730 Cracked Slabs. J STRUCT. ENG., 118(8):2004-2022. [http://118\(8\):2004-](http://118(8):2004-2022.10.1061/(asce)0733-9445(1992)118:8(2004))
731 [2022.10.1061/\(asce\)0733-9445\(1992\)118:8\(2004\)](http://118(8):2004-2022.10.1061/(asce)0733-9445(1992)118:8(2004))
- 732 [33] Xue, D., Liu, Y., Yu, Z., & He J. (2012). Static behavior of multi-stud shear connectors for
733 steel-concrete composite bridge. J. CONSTR. STEEL RES., 74(8):1-7.
734 <http://10.1016/j.jcsr.2011.09.017>
- 735 [34] Li, M. (2015). Refined Calculation Method and Time-Dependent Behaviors of Stud Connectors
736 in Steel-Concrete Composite Girder Bridges. Southeast University.
- 737 [35] Xu, C., Sugiura, K. (2013). FEM analysis on failure development of group studs shear
738 connector under effects of concrete strength and stud dimension. ENG. FAIL. ANAL., 35:343-
739 354. <http://10.1016/j.engfailanal.2013.02.023>
- 740 [36] Dassault Systèmes. Abaqus software Vélizy-Villacoublay, France. <https://www.abaqus.com/>
- 741 [37] Zhao, J., & Nie J. (2009). Nonlinear finite element analysis of steel plate-concrete composite
742 beams, ENG. MECH., 26(4) 105-112.
- 743 [38] Faham, T., Gianluca, R., & Lessandro, Z. (2013). Probabilistic three-dimensional finite element
744 study on composite beams with steel trapezoidal decking. J. CONSTR. STEEL. RES., 80:394-
745 411. <http://10.1016/j.jcsr.2012.10.003>
- 746 [39] Nie J., & Wang Y. (2013). Comparison study of constitutive model of concrete in ABAQUS
747 for static analysis of structures, ENG. MECH., 30 (4): 59-67. (in Chinese)
- 748 [40] Guo, Z., & Shi, X. Principles and analysis of reinforced concrete, Tsinghua University Press,
749 Beijing, China, 2003. (in Chinese)
- 750 [41] MHURD of China. Code for design of concrete structures (GB 50010-2010). CABP, Beijing,
751 China, 2010.
- 752 [42] Hordijk, D. (1992). Tensile and tensile fatigue behaviour of concrete: experiments, modelling
753 and analyses, Heron 37: 3 - 79.

- 754 [43] CEN, Eurocode 3 – Design of steel structures – Part 1-5: Plated structural elements, CEN,
755 Brussels, 2006.
- 756 [44] MHURD of China. Technical code for safety appraisal of engineering structural strengthening
757 materials (GB 50728-2011). CABP, Beijing, China, 2011.
- 758 [45] Luccioni, B.M., López, D.E., & Danesi, R.F. (2005). Bond-slip in reinforced concrete elements.
759 J. STRUCT. ENG., 131(11), 1690-1698. [https://doi.org/10.1061/\(ASCE\)0733-](https://doi.org/10.1061/(ASCE)0733-9445(2005)131:11(1690))
760 9445(2005)131:11(1690)
- 761 [46] Kankam, C.K. (1997). Relationship of bond stress, steel stress, and slip in reinforced concrete.
762 J. STRUCT. ENG., 123(1), 79-85. [https://doi.org/10.1061/\(ASCE\)0733-9445\(1997\)123:1\(79\)](https://doi.org/10.1061/(ASCE)0733-9445(1997)123:1(79))

Author's Manuscript